Technical Report No. 139

4853-19-T

FORCED OSCILLATIONS IN A CLASS OF SELF-BIASED MULTIMODE OSCILLATORS

by

F. N. Bailey

Approved by: B. F. Barton

for

COOLEY ELECTRONICS LABORATORY

Department of Electrical Engineering
The University of Michigan
Ann Arbor

Contract No DA-36-039 sc-89227
U. S. Army Electronics Materiel Agency
Department of the Army Project No. 3A99-06-001-01
Fort Monmouth, New Jersey

March 1964

ABSTRACT

The behavior of a class of multimode oscillators having two nonlinear elements and operating under the influence of an external signal is analyzed using the approximation procedures of Krylov, Bogoliubov and Mitropolsky. Although the features of the basic circuit are chosen to conform to the general characteristics of common self-biased oscillators, the procedures employed are applicable to a large class of problems involving two nonlinear elements.

Through the approximating procedure, the system of nonlinear differential equations describing the basic circuit is replaced by a new, more tractable system of three first-order nonlinear differential equations. Phase space solutions of this approximating system are then used to predict and analyze several interesting features of forced oscillator operation including frequency entrainment, pulling, and superregenerative detection. The results of the theoretical analysis are shown to be in very close agreement with the actual behavior of an experimental oscillator.

LIST OF ILLUSTRATIONS

Figure	Title	Page
1	Basic equivalent circuit for the class of oscillators under consideration.	2
2	A typical self-biased oscillator with external signal.	2
3	Illustration of the level curves of the $\dot{E}_c = 0$ and $\dot{E} = 0$ surfaces near an equilibrium point of the unforced system.	10
4	Lock-in region in (A, Δ_1) parameter space as predicted by the mathematical model.	12
5	Typical intersection of the $\dot{E}_c = 0$ and $\dot{E} = 0$ surfaces showing variation in E_p and E_{cp} along the intersection curve and the equilibrium points P^o, P, P'.	13
6	Possible operating path near stable equilibrium point when (29) is not satisfied.	14
7	Assumed $i(e_c)$ and $i_c(e_c)$ characteristics.	17
8	Conductance characteristics corresponding to Fig. 7.	17
9	Determination of dependence of g_m on γ.	18
10	Predicted $\dot{E} = 0$ and $\dot{E}_c = 0$ contours in the (E, E_c)-plane of the unforced oscillator when $G_g = 150$ μmho [note that $\dot{E} = 0$ along the entire E_c-axis — see (19)].	20
11	Section of the (E, E_c, θ)-phase space along the $\dot{E}_c = 0$ surface (in this case the $\dot{E}_c = 0$ surface is a plane).	21
12	Typical E vs. Δ equilibrium point locus. Injected signal A as a parameter.	22
13	Predicted and observed lock-in characteristics for oscillator with stable equilibrium point in (x, Δ)-coordinates.	24
14	Predicted and observed lock-in region boundaries in (A, Δ)-plane.	25
15	Typical unforced system (E, E_c)-phase plane configuration showing limit cycles and regions R_1 and R_2.	26
16	Conductance function $G_T(t)$ vs. t and a linear approximation.	31
17	Comparison of two frequency dependent terms in the forced response.	17

LIST OF ILLUSTRATIONS (Cont.)

Figure	Title	Page
18	Comparison of predicted and observed detector output E_{cm} versus injected signal amplitude A at several frequency separations Δ.	36
19	Detector output E_{cm} versus frequency separation Δ with fixed injected signal amplitude.	36
20	Predicted and observed sensitivity of E_{cm} to changes in A showing decrease in observed sensitivity at several values of frequency separation Δ.	37

TABLE OF CONTENTS

		Page
	ABSTRACT	ii
	LIST OF ILLUSTRATIONS	iii
1.	INTRODUCTION	1
2.	DEVELOPMENT OF THE MATHEMATICAL MODEL	2
3.	QUALITATIVE FEATURES OF THE MODEL	8
	3.1 Equilibrium Points	9
	3.2 Operation of the Forced System Near Stable Equilibrium Points of the Unforced System	12
	3.3 Operation of the Forced System When the Unforced System Has a Limit Cycle	14
4.	ANALYSIS OF A SPECIFIC OSCILLATOR AND COMPARISON WITH EXPERIMENTAL RESULTS	16
	4.1 Computation of the Functions G_m^{hf}, G_c^{hf}, $G_c^{\ell f}$, and β	16
	4.2 Operation of the Forced System When the Unforced System Has a Stable Equilibrium Point and $\dot{A} = 0$	19
	4.3 Forced Oscillations When the Unforced System Has a Stable Limit Cycle	26
	4.4 Sensitivity and Superregenerative Detection	34
5.	CONCLUSIONS	38
	APPENDIX	39
	REFERENCES	42
	DISTRIBUTION LIST	43

1. INTRODUCTION

In a recent paper, Bailey and Naylor (Ref. 1) presented an analysis of the undisturbed behavior of a class of oscillators modeled by a circuit containing two nonlinear elements. That particular class was chosen for analysis because it included the frequently encountered self-biased oscillators. In this report the analysis will be extended to include the behavior of the chosen class of oscillators in the presence of external signals.

As in the previous analysis (Ref. 1), a mathematical model for the class of oscillators under consideration is chosen with the aid of the approximation techniques of Krylov, Bogoliubov, and Mitropolsky (Ref. 2). When the forcing signal is absent, this model reduces to the unforced model considered in Reference 1. With the forcing signal present the model is used to predict several features of forced oscillations in self-biased oscillators (e.g., lock-in, pulling, superregenerative detection) with considerable accuracy. In addition, the concepts developed are applied to an analysis of the operation of self-quenched superregenerative detectors and an application to nonlinear externally quenched (logarithmic) detectors is indicated. These latter results are an extension of previous superregenerative detector analysis carried out by Whitehead (Ref. 3).

The contents of this paper are arranged as follows: (a) in the second section the mathematical model is developed, (b) in the third section the qualitative features of the model are examined, and (c) in the fourth section a specific oscillator circuit is subjected to a detailed quantitative analysis. Certain fundamental conclusions of this analysis are supported by experimental results.

2. DEVELOPMENT OF THE MATHEMATICAL MODEL

The mathematical model is developed for devices described by the equivalent circuit shown in Fig. 1. The oscillator with external signal shown in Fig. 2 is an example of a system with this equivalent circuit. The circuits of Figs. 1 and 2 are equivalent when (1) the tank Q is high (i. e., two of the poles of the linear part are near the $j\omega$-axis) and (2) the characteristics of the nonlinear current sources in Fig. 1 have been chosen to approximate the grid and plate characteristics of the tube. A complete discussion of this equivalence is given in Reference 1.

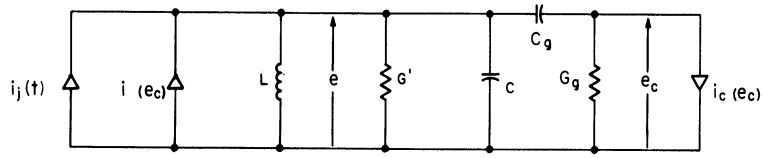

Fig. 1. Basic equivalent circuit for the class of oscillators under consideration.

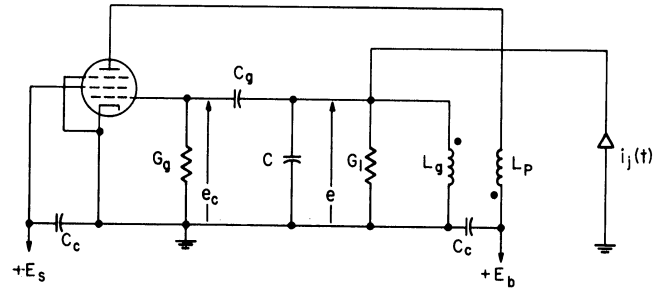

Fig. 2. A typical self-biased oscillator with external signal.

The circuit of Fig. 1 is described by the system of differential equations:

$$\begin{cases} G'e + C\dot{e} + \frac{1}{L}\int e\,dt + C_g(\dot{e}-\dot{e}_c) = i(e_c) + i_j(t)\ , \\ G_g e_c + C_g(\dot{e}_c-\dot{e}) + i_c(e_c) = 0\ . \end{cases} \tag{1}$$

With the introduction of the new variable $b = \dot{e}$, the following system of three first-order equations is obtained as an equivalent to (1):

$$\begin{cases} \dot{e} = b \ , \\ \dot{e}_c = b - \dfrac{G_g}{C_g} e_c - \dfrac{1}{C_g} i_c(e_c) \ , \\ \dot{b} = -\dfrac{1}{C}[G + g_c(e_c) - g_m(e_c)]\, b - \dfrac{1}{LC} e \\ \qquad + \dfrac{1}{CC_g}[G_g + g_c(e_c) - g_m(e_c)]\,[G_g e_c + i_c(e_c)] + \dfrac{1}{C} i_j(t) \ , \end{cases} \tag{2}$$

where

$$G = G' + G_g \ , \tag{3}$$

$$g_c(e_c) = \frac{di_c(e_c)}{de_c} \ , \tag{4}$$

$$g_m(e_c) = \frac{di(e_c)}{de_c} \ . \tag{5}$$

The last two relations define the equivalent nonlinear grid conductance and plate transconductance, respectively.

Two further assumptions will be made: (a) $i_j(t) = A(t) \cos \nu t$ where A(t) is a nonnegative, slowly varying function of time[1] and ν is a constant near $\omega_o = 1/\sqrt{LC}$, and (b) $Q = \omega_o C/G > 10$ or, equivalently, the damping ratio is less than .05. The system (2), subject to restrictions (a) and (b), now gives a mathematical description of the problem at hand.

Because of the high-Q assumption, it is anticipated that $e_c(t)$ will be of the form

$$e_c(t) = E_c(t) + E(t) \cos[\nu t + \theta(t)] \ , \tag{6}$$

where E_c, E, and θ are constants or slowly varying functions (cf. CW oscillation and squegging oscillation). The form of $e_c(t)$ assumed in (6) corresponds to a separation into a low-frequency bias component, E_c, and a high frequency component, $E \cos(\nu t + \theta)$.

---

[1] While the mathematical model obtained is valid for time-varying A, the analysis of the model, in this report, will generally be restricted to the case where A is a constant. An exception is the superregenerative detector analysis considered in Section 4.3 where A may be time-variable.

Since a direct solution of (2) is not readily obtained by techniques which yield insight into over-all oscillator behavior, it is advantageous to choose a new, more tractable system of differential equations which approximates (2) in some sense. The procedure for selecting the approximating system is suggested by the work of Krylov, Bogoliubov, and Mitropolsky (Ref. 2). An analytical investigation of the fidelity of approximation will not be attempted, but experience has shown (see Ref. 2) that this procedure is frequently successful in treating this type of problem. In addition, the experimental results described in Section 4 corroborate much of the analysis.

The anticipated form of the solution (6) suggests the following change of variables:

$$\begin{cases} e = E\cos\gamma\ , \\ e_c = E_c + E\cos\gamma\ , \\ b = -E\nu\sin\gamma\ , \end{cases} \tag{7}$$

with $\gamma = \nu t + \theta$. The Jacobian of this transformation is $-E\nu$, showing that the transformation is one-to-one and has an inverse at all points away from the plane $E = 0$.

The transformation is carried out by substituting (7) into (2) and making use of the fact that $\nu t = \gamma - \theta$. The resulting system in E, E_c, γ, and θ is

$$\begin{cases} \dot{E} = -\frac{E}{C}\left[G + g_c(E_c + E\cos\gamma) - g_m(E_c + E\cos\gamma)\right]\sin^2\gamma + \frac{\omega_o^2-\nu^2}{\nu}E\sin\gamma\cos\gamma \\ \quad - \frac{G_g}{CC_g\nu}\left[G_g + g_c(E_c + E\cos\gamma) - g_m(E_c + E\cos\gamma)\right]\left[E_c\sin\gamma - E\sin\gamma\cos\gamma\right] \\ \quad - \frac{1}{CC_g\nu}\, i_c(E_c + E\cos\gamma)\left[G_g + g_c(E_c + E\cos\gamma) - g_m(E_c + E\cos\gamma)\right]\sin\gamma \\ \quad + \frac{A(t)}{C}\sin(\gamma - \theta)\sin\gamma\ , \\ \dot{E}_c = -\frac{G_g}{C_g}E_c - \frac{G_g}{C_g}E\cos\gamma - \frac{1}{C_g}\, i_c(E_c + E\cos\gamma)\ , \\ \dot{\gamma} = \nu - \frac{1}{C}\left[G + g_c(E_c + E\cos\gamma) - g_m(E_c + E\cos\gamma)\right]\sin\gamma\cos\gamma + \frac{\omega_o^2-\nu^2}{\nu}\cos^2\gamma \\ \quad - \frac{G_g}{CC_gE\nu}\left[G_g + g_c(E_c + E\cos\gamma) - g_m(E_c + E\cos\gamma)\right]\left[E_c\cos\gamma + E\cos^2\gamma\right] \\ \quad - \frac{1}{CC_gE\nu}\, i_c(E_c + E\cos\gamma)\left[G_g + g_c(E_c + E\cos\gamma) - g_m(E_c + E\cos\gamma)\right]\cos\gamma \\ \quad + \frac{A(t)}{CE}\sin(\gamma - \theta)\cos\gamma\ . \end{cases} \tag{8}$$

Note that (8) is still an exact mathematical description of Fig. 1, but this description is now expressed in terms of the new variables E, E_c, γ, and θ. The approximating system is now chosen to approximate (8) under the assumption that E, E_c, θ, and A are slowly varying functions of time. When this assumption is justified, the variables E, E_c, θ, and A may be assumed constant in an averaging of (8) over one RF period (approximately $2\pi/\omega_o$). Completion of this averaging yields the approximating system[2]

$$\begin{cases} \dot{E} = \frac{E}{2C}\left[G_m^{hf}(E, E_c) - G_c^{hf}(E, E_c) - G\right] + \frac{A(t)}{2C}\cos\theta \ , \\ \dot{E}_c = -\frac{E_c}{C_g}\left[G_g + G_c^{\ell f}(E, E_c)\right] \ , \\ \dot{\gamma} = \nu + \frac{\omega_o^2 - \nu^2}{2\nu} - \beta'(E, E_c, \nu) - \frac{A(t)}{2CE}\sin\theta \ , \end{cases} \tag{9}$$

where

$$G_m^{hf}(E, E_c) = \frac{1}{\pi}\int_0^{2\pi} g_m(E_c + E\cos\lambda)\sin^2\lambda\, d\lambda \ , \tag{10}$$

$$G_c^{hf}(E, E_c) = \frac{1}{\pi}\int_0^{2\pi} g_c(E_c + E\cos\lambda)\sin^2\lambda\, d\lambda \ , \tag{11}$$

$$G_c^{\ell f}(E, E_c) = \frac{1}{2\pi E_c}\int_0^{2\pi} i_c(E_c + E\cos\lambda)\, d\lambda \ , \tag{12}$$

$$\beta'(E, E_c, \nu) = \frac{1}{2\pi}\int_0^{2\pi} \frac{G_g}{CC_g\nu}\left\{G_g\cos\lambda + \left[g_c(E_c + E\cos\lambda) - g_m(E_c + E\cos\lambda)\right]\left[\frac{E_c}{E} + \frac{i_c(E_c + E\cos\lambda)}{G_g} + \cos\lambda\right] + i_c(E_c + E\cos\lambda)\right\}\cos\lambda\, d\lambda \ . \tag{13}$$

A further simplification is obtained by assuming that the angular frequencies ω_o and ν are similar; that is, by assuming that $|\Delta/\omega_o| << 1$, where

$$\Delta = \omega_o - \nu \ . \tag{14}$$

In this case

$$\frac{\omega_o^2 - \nu^2}{2\nu} \approx \omega_o - \nu = \Delta \tag{15}$$

---

[2] See Appendix for details of the approximation procedure. The terms G_m^{hf}, G_c^{hf}, and $G_c^{\ell f}$ in (9) may be interpreted as voltage dependent nonlinear conductances. For a complete discussion see Refs. 1 or 6.

and it is possible to define

$$\beta(E, E_c) = \frac{\nu}{\omega_o} \beta'(E, E_c, \nu) \tag{16}$$

which is almost equivalent to β', but explicitly independent of ν. Finally, it is convenient to define

$$\omega(E, E_c) = \omega_o - \beta(E, E_c) , \tag{17}$$

and note that

$$\dot{\theta} = \dot{\gamma} - \nu , \tag{18}$$

so that the final form of the approximating system is

$$\begin{cases} \dot{E} = \frac{E}{2C} [G_m^{hf}(E, E_c) - G_c^{hf}(E, E_c) - G] + \frac{A(t)}{2C} \cos\theta , & (19) \\ \dot{E}_c = -\frac{E_c}{C_g} [G_g + G_c^{\ell f}(E, E_c)] , & (20) \\ \dot{\theta} = \omega(E, E_c) - \nu - \frac{A(t)}{2CE} \sin\theta . & (21) \end{cases}$$

These three equations are an approximating system which describes the circuit of Fig. 1 under the assumptions mentioned above. For convenience the right-hand sides of (19), (20) and (21) will often be denoted by $f_1(E, E_c, \theta)$, $f_2(E, E_c)$, and $f_3(E, E_c, \theta)$, respectively. Analysis of this mathematical model for the oscillator will be the subject of much of the remainder of this paper. The sections which follow will consider the behavior predicted by this model and the validity of these predictions.

Before proceeding it is worthwhile to note the assumptions that are implicit in the stipulation that E, E_c and A be slowly varying functions. These assumptions imply that:

(a) $\left|\frac{\dot{E}}{E}\right| \frac{2\pi}{\omega_o} << 1 ,$

(b) $\left|\frac{\dot{E}_c}{E_c}\right| \frac{2\pi}{\omega_o} << 1 ,$

(c) $\frac{|\dot{\theta}|}{\omega_o} << 1 ,$

(d) $\left|\frac{\dot{A}}{A}\right| \frac{2\pi}{\omega_o} << 1 .$

Examination of (19) reveals that (a) introduces a restriction on the size of A which may be handled by these methods. Thus, it will generally be assumed that A is small. This is compatible with a majority of actual situations in which an oscillator operates in the presence of an external signal.

3. QUALITATIVE FEATURES OF THE MODEL

The oscillator mathematical model described by (19), (20), and (21) is a system of three first-order, nonlinear, differential equations. The solutions may be divided into two classes: (a) unforced oscillations when A = 0 and (b) forced oscillations when $A \neq 0$.

Consider first the case of unforced oscillation. When A = 0, (19) and (20) describe a second-order system independent of θ and capable of solution in the (E, E_c)-phase plane. The resulting E(t) and $E_c(t)$ can be substituted into (21). Integration then gives

$$\theta(t) = (\omega_o - \nu)t + \int_o^t \beta[E(z), E_c(z)]\,dz + \theta_o , \tag{22}$$

where θ_o is the initial condition $\theta(0)$. The E(t), $E_c(t)$, and $\theta(t)$ which result may then be transformed back into e, e_c, and b variables from (7), giving

$$e_c(t) = E_c(t) + E(t)\cos[\omega_o t + \int_o^t \beta(E, E_c)\,dz + \theta_o] . \tag{23}$$

This unforced solution (note that the basic angular frequency is now ω_o) was the subject of previous discussion in Reference 1.[3]

When $A \neq 0$ but $\dot{A} = 0$ the solutions of the third-order system may be represented in an (E, E_c, θ)-phase space. In order to avoid the difficulties associated with the representation of 3-space curves on plane paper, (E, E_c)-plane projections (orthogonal) of three-dimensional curves and level curves [see Kaplan Ref. 4] of three-dimensional surfaces

---

[3] In Ref. 1 it was assumed, for convenience, that $\int_o^t \beta(E, E_c)\,dz + \theta_o \equiv 0$. Although this did not effect the resulting amplitudes E(t) and $E_c(t)$ [since (19) and (20) are independent of θ when A = 0] , it failed to give a picture of oscillator frequency shifts during operation. In addition it was stated in Ref. 1 that the $\theta(t)$ results obtainable from (21) [with A = 0] were not a satisfactory approximation to the actual $\theta(t)$. The $\theta(t)$ obtained in this paper is still in quantitative disagreement with several known features of oscillator performance. However, because it shows proper qualitative behavior it is used, as necessary, to obtain solutions.

will be used wherever possible. Since the forced behavior for small A is found to be strongly dependent on and quite similar to the behavior of the corresponding unforced system (the unforced system with identical parameters), the effects of the forcing function can be described in many cases as modifications of the unforced (E, E_c)-phase trajectories. When both A and $\dot{A}$ are nonzero, the problem is even more difficult. Hence, detailed treatment of this case will be limited to a few specific situations. Finally note that the form of the coordinate transformation (7) insures that all behavior of interest will be found in the region $-\pi < \theta \leq \pi$ and $E \geq 0$.

3.1 Equilibrium Points

When $A = 0$ the second-order system (unforced system) has equilibrium points at the intersection of the $\dot{E} = 0$ and $\dot{E}_c = 0$ loci [plane curves in the (E, E_c)-plane]. These points are solutions of the system

$$\begin{cases} f_1(E, E_c, 0) = 0, \\ f_2(E, E_c) = 0. \end{cases} \tag{24}$$

When $A \neq 0$ but $\dot{A} = 0$ the third-order system (forced system) has equilibrium points at the intersection of the $\dot{E} = 0$, $\dot{E}_c = 0$, and $\dot{\theta} = 0$ loci [surfaces in (E, E_c, θ)-space]. These points are solutions of the system

$$\begin{cases} f_1(E, E_c, \theta) = 0, \\ f_2(E, E_c) = 0, \\ f_3(E, E_c, \theta) = 0. \end{cases} \tag{25}$$

Since f_2 is independent of θ, the $\dot{E}_c = 0$ surface is a cylinder with its axis parallel to the θ-axis (i.e., its level curves are identical for all θ). This cylindrical surface may be described as $E_c = g(E)$ and its intersection with the $\dot{E} = 0$ surface is characterized by the additional equation $f_1[E, g(E), \theta] = 0$. Note that in the $\dot{E}_c = 0$ surface at the intersection with the $\dot{E} = 0$ surface

$$\left.\frac{dE}{d\theta}\right|_{E_c = g(E)} = \frac{-\dfrac{\partial f_1}{\partial \theta}}{\dfrac{\partial f_1}{\partial E} + \dfrac{\partial f_1}{\partial E_c} \cdot \dfrac{dg}{dE}} = \frac{A \dfrac{\sin \theta}{2C}}{h(E, E_c)}, \tag{26}$$

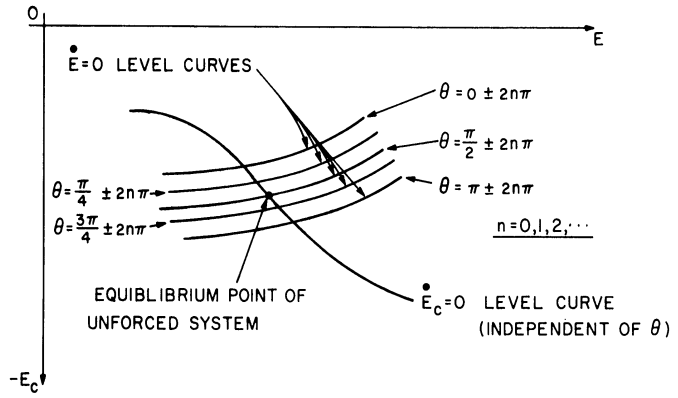

Fig. 3. Illustration of the level curves of the $\dot{E}_c = 0$ and $\dot{E} = 0$ surfaces near an equilibrium point of the unforced system.

where the definition of the new function $h(E, E_c)$ is obvious. Since $h(E, E_c)$ is bounded and independent of A and θ, and A has been assumed small, the oscillation in $dE/d\theta$ as a function of θ noted in (26) indicates that the $\dot{E} = 0$ surface at the intersection with the $\dot{E}_c = 0$ surface may be viewed as a portion of a slightly rippled cylinder with axis parallel to the θ-axis and ripple amplitude proportional to A. The level curves for such $\dot{E} = 0$ surface are shown in Fig. 3.

The above argument suggests that the intersection of the $\dot{E} = 0$ and $\dot{E}_c \neq 0$ surfaces is a set of wavy vertical lines with one line rising above each equilibrium point of the unforced system. Equilibrium points of the forced system will then lie on these lines at points where $f_3(E, E_c, \theta) = 0$. That is, at points where

$$\omega(E_p, E_{cp}) - \nu = \frac{A}{2CE_p} \sin \theta_p \quad , \tag{27}$$

with (E_p, E_{cp}, θ_p) being the coordinates of the forced equilibrium point. When A is small the ripples in the $\dot{E} = 0$, $\dot{E}_c = 0$ intersection lines are small enough that $E_p \approx E_p^o$ and $E_{cp} \approx E_{cp}^o$ where E_p^o and E_{cp}^o are the coordinates of the corresponding unforced equilibrium point. For this condition, (27) may be rewritten as

$$\omega_1 - \nu = \frac{A}{2CE_p^o} \sin \theta_p \, , \tag{28}$$

where $\omega_1 = \omega(E_p^o, E_{cp}^o)$. This equation will have zero, one, or two solutions in the interval $-\pi < \theta_p \leq \pi$. Thus, for small A, a necessary condition for existence of an equilibrium point of the forced system of differential equations is

$$\left|\omega_1 - \nu\right| \leq \frac{A}{2CE_p^o} \,. \tag{29}$$

This is the relation between A and $|\omega_1-\nu|$ that must exist if an equilibrium point is to occur.

When an equilibrium points exists, its stability will depend on the characteristic roots of the linearized system matrix

$$\begin{bmatrix} f_{1E} & f_{1E_c} & f_{1\theta} \\ f_{2E} & f_{2E_c} & 0 \\ f_{3E} & f_{3E_c} & f_{3\theta} \end{bmatrix} \tag{30}$$

where $f_{ij} = \partial f_i/\partial j$ is evaluated at the equilibrium point with i = 1, 2, 3 and j = E, E_c, θ. These roots are the roots of the characteristic equation

$$[(f_{1E} - \lambda)(f_{2E_c} - \lambda) - f_{1E_c} f_{2E}][f_{3\theta} - \lambda] + f_{1\theta}[f_{2E} f_{3E_c} - f_{3E}(f_{2E_c} - \lambda)] = 0 \,. \tag{31}$$

Since

$$f_{1\theta} = -\frac{A}{2C}\sin\theta \,, \tag{32}$$

(31) describes a Root Locus [see Ref. 5] problem in the parameter A. Thus, the roots of (31) will be near the roots of the simplified form

$$[f_{3\theta} - \lambda][(f_{1E} - \lambda)(f_{2E_c} - \lambda) - f_{1E_c} f_{2E}] = 0 \tag{33}$$

when A is sufficiently small. Stability is then approximately determined by the real parts of $f_{3\theta}$ and the characteristic roots of the corresponding unforced system equilibrium point.

In summary, equilibrium points of the system (25) will occur above the (E, E_c)-plane equilibrium points of the unforced system at points where (28) is satisfied. When A is small, the (E, E_c)-plane projections of the forced equilibrium points will be quite close to the corresponding equilibrium points of (24). Moreover, for small A an equilibrium point of the forced system will be stable if $f_{3\theta}$ is negative and the corresponding unforced equilibrium point is also stable. Note the close dependence of the forced and unforced behavior.

3.2 Operation of the Forced System Near Stable Equilibrium Points of the Unforced System

Assume that (E_p^o, E_{cp}^o) are the coordinates of a stable equilibrium point, P^o, of the unforced system. The behavior of solutions of the forced system near this point will depend on whether (29) is satisfied.

If (29) is satisfied there will be two equilibrium points[4] in the (E, E_c, θ)-space above or below the (E, E_c)-plane [see (28)]. From the above stability conditions and the fact that

$$f_{3\theta} = -\frac{A}{2CE}\cos\theta \ , \tag{34}$$

it is clear that one point, P, will be stable and one point, P', will be unstable. Operation at

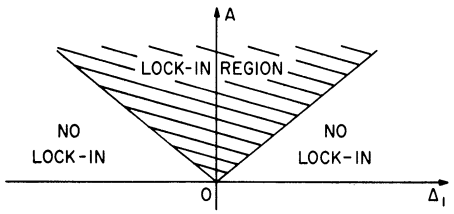

Fig. 4. Lock-in region in (A, Δ_1) parameter space as predicted by the mathematical model.

the stable equilibrium point (E_p, E_{cp}, θ_p) gives a predicted oscillator grid voltage

$$e_c(t) = E_{cp} + E_p \cos(\nu t + \theta_p) \ . \tag{35}$$

This fixed amplitude and phase operation in the mathematical model corresponds to what is commonly called lock-in or frequency entrainment of the oscillator by the external signal. The region of lock-in depends on A and $\Delta_1 = \omega_1 - \nu$ satisfying (29). As A increases, the "lock-in bandwidth" or range of possible frequency entrainment specified by Δ_1 increases as shown in Fig. 4.

During lock-in the phase of the forced oscillation relative to the unforced oscillation, θ_p, varies with A and Δ_1 as described by (28). The induced variations in θ_p cause the equilibrium point to move along the wavy $\dot{E} = 0$, $\dot{E}_c = 0$ intersection line producing

[4] In the special case where $|\omega_1 - \nu| = A/2CE_p^o$ there is only one equilibrium point but this situation is structurally unstable and not considered here.

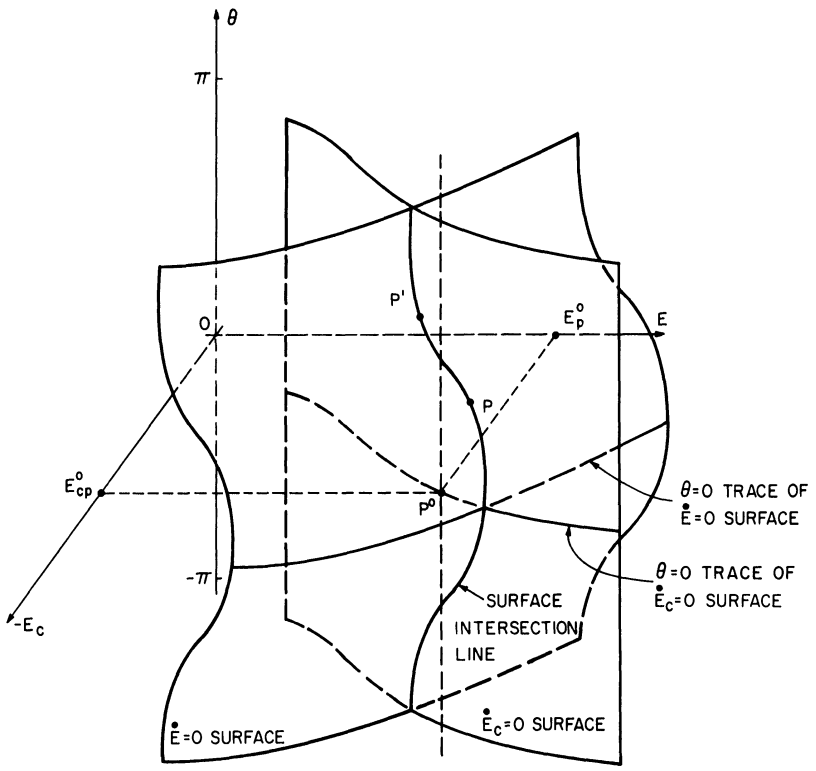

Fig. 5. Typical intersection of the $\dot{E}_c = 0$ and $\dot{E} = 0$ surfaces showing variation in E_p and E_{cp} along the intersection curve and the equilibrium points P^o, P, P'.

variations in E_p and E_{cp} typical of lock-in phenomena. A typical pattern is shown in Fig. 5. For a specific oscillator these variations may be used to construct the well-known lock-in characteristics of E vs. Δ_1 with A as a parameter. This is carried out in Section 4.

When (29) is not satisfied at (E_p^o, E_{cp}^o), a new form of behavior is encountered. Since the equilibrium point of (19) and (20) is still stable for each fixed θ, the fixed θ solutions of these equations converge toward a corresponding equilibrium point. However, $\dot{\theta}$ remains positive (or negative) and θ continually increases (or decreases) causing this equilibrium point to move up (or down) through the phase space along the intersection line of the $\dot{E}_c = 0$ and $\dot{E} = 0$ surfaces. Roughly speaking, the convergence of the solutions toward this moving equilibrium point may be expected to produce spiral solution paths in the phase space. This spiral should appear somewhat like that shown in Fig. 6. This behavior appears to correspond to the combination oscillations encountered outside the lock-in region of oscil-

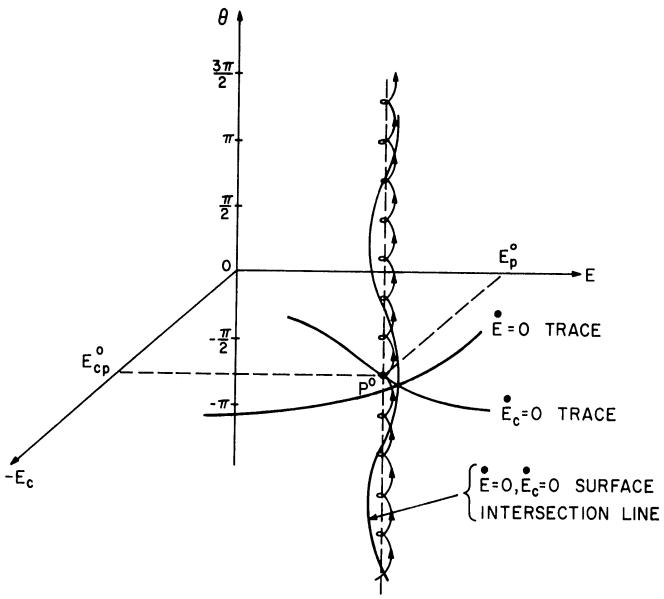

Fig. 6. Possible operating path near stable equilibrium point when (29) is not satisfied.

lators. Note that both amplitude and phase modulation of $e_c(t)$ occur as E and θ vary along the spiral path. This phenomenon will be examined further in a later section.

3.3 Operation of the Forced System When the Unforced System Has A Limit Cycle

When the unforced mathematical model has a (E, E_c)-plane limit cycle the behavior of the forced model becomes considerably more complex. Assuming that the solutions are continuous in the parameter A, it appears reasonable to conclude that when A is small the (E, E_c)-plane projection of the (E, E_c, θ)-space solution path will lie close to the unforced limit cycle. Whether the (E, E_c, θ)-space solution path is itself a limit cycle depends on whether it is closed on itself and this is not easily determined. However, considering only the (E, E_c)-plane projection of this solution path, several comments may be made.

First, because of the way the external signal term enters (19), it appears that when A is small the only significant effect of the forcing term will occur when $\dot{E}$ is also small. That is, the $A/2C \cos \theta$ term in (19) is important only when the operating path is near the $\dot{E} = 0$ contour of the unforced system where $[G_m^{hf} - G_c^{hf} - G]$ is small.

Second, the rewriting of (19) in the form

$$\frac{dE}{E} = \left[\frac{G_m^{hf} - G_c^{hf} - G}{2C} + \frac{A}{2CE} \cos \theta \right] dt \tag{36}$$

suggests that E will be much more sensitive to A in regions where E is also small. The E^{-1} factor in the second term indicates that this term will dominate when E is small causing an increased sensitivity of E to A in such regions.

A more complete discussion of operation in the case of a limit cycle will be possible in the next section. There it will be shown that the above two effects combine to give the superregenerative sensitivity of oscillators exhibiting certain types of limit cycles.

4. ANALYSIS OF A SPECIFIC OSCILLATOR AND COMPARISON WITH EXPERIMENTAL RESULTS

In this section the model and concepts developed above will be applied to the analysis of a specific oscillator configuration. This will serve the twofold purpose of giving further insight into oscillator behavior and providing quantitative results which can be subjected to experimental verification. With this latter end in mind the nonlinear current sources $i(e_c)$ and $i_c(e_c)$ will be chosen to approximate the grid and plate current characteristics of a vacuum tube to be used in a circuit like that shown in Fig. 2.

The experimental oscillator and measuring techniques are essentially the same as the ones described in Ref. 6. The external signal is applied to the oscillator tank from a HP-606 signal generator through a 100KΩ resistor.

4.1 Computation of the Functions G_m^{hf}, G_c^{hf}, $G_c^{\ell f}$, and β

The $i(e_c)$ and $i_c(e_c)$ characteristics will be chosen as

$$i(e_c) = \begin{cases} 0 & \text{for } e_c \leq S \\ -\frac{G_m}{2S}(S-e_c)^2 & \text{for } S \leq e_c \leq 0 \\ G_m e_c & \text{for } 0 \leq e_c \end{cases} \tag{37}$$

$$i_c(e_c) = \begin{cases} 0 & \text{for } e_c \leq 0 \\ G_c e_c & \text{for } e_c \geq 0 \end{cases} \tag{38}$$

where S, G_m, and G_c are parameters. These functions are illustrated in Fig. 7. The functions $i(e_c)$ and $i_c(e_c)$ are clearly similar to the grid and plate current characteristics of a pentode.

The corresponding conductances are

$$g_m(e_c) = \frac{di(e_c)}{de_c} = \begin{cases} 0 & \text{for } e_c \leq S \\ G_m(1 - \frac{e_c}{S}) & \text{for } S \leq e_c < 0 \\ G_m & \text{for } e_c \geq 0 \end{cases} \tag{39}$$

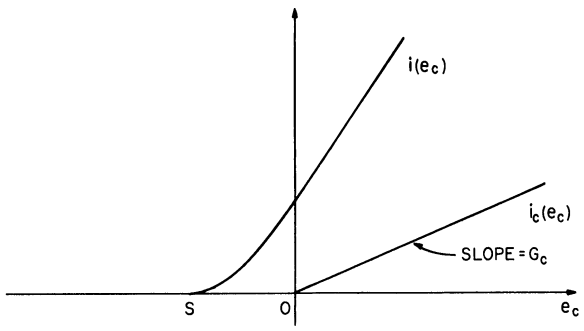

Fig. 7. Assumed $i(e_c)$ and $i_c(e_c)$ characteristics.

$$g_c(e_c) = \frac{di_c(e_c)}{de_c} = \begin{cases} 0 & \text{for } e_c < 0 \\ G_c & \text{for } e_c > 0 \end{cases} . \tag{40}$$

The $g_m(e_c)$ and $g_c(e_c)$ functions are illustrated in Fig. 8. The relations (38), (39), (40), and the transformation $e_c = E_c + E \cos \gamma$ can now be inserted into (10), (11), (12), and (13) to give the desired relations G_m^{hf}, etc. However, the integration involved is simplified by the definition of the two conduction angles

$$\sigma = \begin{cases} \cos^{-1}\left(\frac{S-E_c}{E}\right) & \text{for } E \geq |S-E_c| \\ 0 & \text{for } E_c \leq S \text{ and } E < |S-E_c| \\ \pi & \text{for } E_c \geq S \text{ and } E < |S-E_c| \end{cases} \tag{41}$$

$$\phi = \begin{cases} \cos^{-1}\left(\frac{-E_c}{E}\right) & \text{for } E \geq |E_c| \\ 0 & \text{for } E_c < 0 \text{ and } E < |E_c| \\ \pi & \text{for } E_c > 0 \text{ and } E < |E_c| \end{cases} . \tag{42}$$

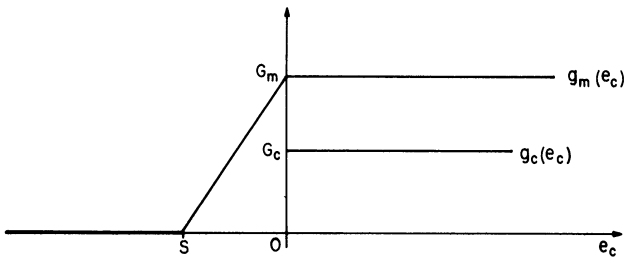

Fig. 8. Conductance characteristics corresponding to Fig. 7.

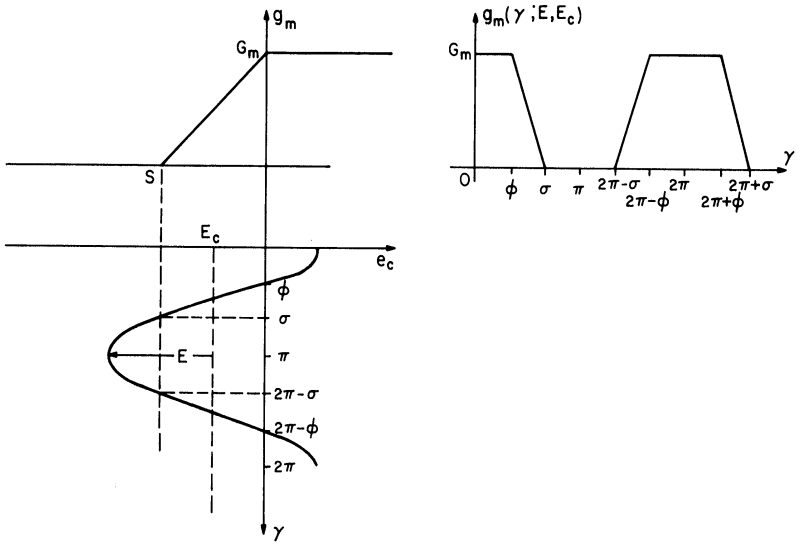

Fig. 9. Determination of dependence of g_m on γ.

The use of these conduction angles is illustrated in Fig. 9. There they are used to give a convenient definition of $g_m(E_c + E\cos\gamma)$ in terms of γ only (E, E_c are considered parameters in the integration). A similar procedure may be employed with g_c and i_c.

With the aid of the ideas presented in Fig. 9 the integrals (10), (11), (12), and (13) can be evaluated. This gives

$$G_m^{hf}(E, E_c) = \frac{G_m}{\pi} f(\sigma) + \frac{KE_c}{\pi}[f(\sigma) - f(\phi)] + \frac{2KE}{3\pi}[\sin^3\sigma - \sin^3\phi], \tag{43}$$

$$G_c^{hf}(E, E_c) = \frac{G_c}{\pi} f(\phi), \tag{44}$$

$$G_c^{\ell f}(E, E_c) = \frac{G_c}{\pi}\left(\phi + \frac{E}{E_c}\sin\phi\right), \tag{45}$$

$$\beta(E, E_c) = \frac{G_g^2}{2CC_g\omega_o} + \frac{1}{2CC_g\omega_o\pi}\left\{[G_g(2G_c + KE_c) + G_c(G_c - G_m)]\left[\frac{2E_c}{E}\sin\phi + h(\phi)\right]\right.$$
$$\left. - G_g[G_m + KE_c]\left[\frac{2E_c}{E}\sin\sigma + h(\sigma)\right]\right\}, \tag{46}$$

where

$$K = -G_m/S,$$
$$f(x) = x - (1/2)\sin 2x,$$
$$h(x) = x + (1/2)\sin 2x.$$

The computation of these functions completes the adaptation of the model to the specified nonlinear characteristics.

4.2 Operation of the Forced System When the Unforced System Has A Stable Equilibrium Point and $\dot{A} = 0$

With the computation of G_m^{hf}, G_c^{hf}, $G_c^{\ell f}$, and β, the general model (19), (20), and (21) is specialized to circuits having the specific nonlinearities assumed in Section 4.1. The model now describes such circuits in terms of the parameters G_m, G_c, G, C, C_g, and S. When numerical results are required, these parameters will be assumed to have the following values:

$$\begin{aligned} G_m &= 2400\ \mu\text{mho}, \\ G_c &= 2000\ \mu\text{mho}, \\ G &= G' + G_g, \\ G' &= 250\ \mu\text{mho}, \\ C &= 300\ \text{pf}, \\ C_g &= 1000\ \text{pf}, \\ S &= -3\ \text{volts} \end{aligned} \tag{47}$$

(The parameter G_g will be allowed to take on several values in the different examples which follow.) The values chosen in (47) correspond to the measured parameters of the experimental oscillator.

When G_g is large it can be shown (see Ref. 1) that the unforced system has one stable equilibrium point, $P^o = (E_p^o, E_{cp}^o)$, corresponding to a constant amplitude or CW mode of oscillation and one unstable equilibrium point located at the origin (0, 0). For example, when $G_g = 150\ \mu$mho and parameters (47) are assumed, the $\dot{E} = 0$ and $\dot{E}_c = 0$ loci in the (E, E_c)-plane shown in Fig. 10 intersect at point P^o and at the origin. A check of the characteristic roots of the linearized equations shows that in this case the equilibrium point P^o is a stable focus. Thus the solution trajectories (such as T in Fig. 10) near P^o spiral toward the equilibrium point. In fact, a complete plot of the (E, E_c)-phase plane shows that with these parameters almost all initial conditions give solutions which spiral toward P^o.

Consider now the same system with a forcing signal present. If $|\omega(E, E_c)-\nu|$ and A are such that (29) can be satisfied in the vicinity of E_p^o, the forced system will also have a stable equilibrium point. The equilibrium points of the forced system associated with P^o will be located on the curve formed by the intersection of the $\dot{E} = 0$ and $\dot{E}_c = 0$ surfaces above P^o at points (E_p, E_{cp}, θ_p) which are also solutions of (27). These points may be located by noting that when A is small, $E_p \approx E_p^o$, $E_{cp} \approx E_{cp}^o$ and θ_p may be obtained from a modified

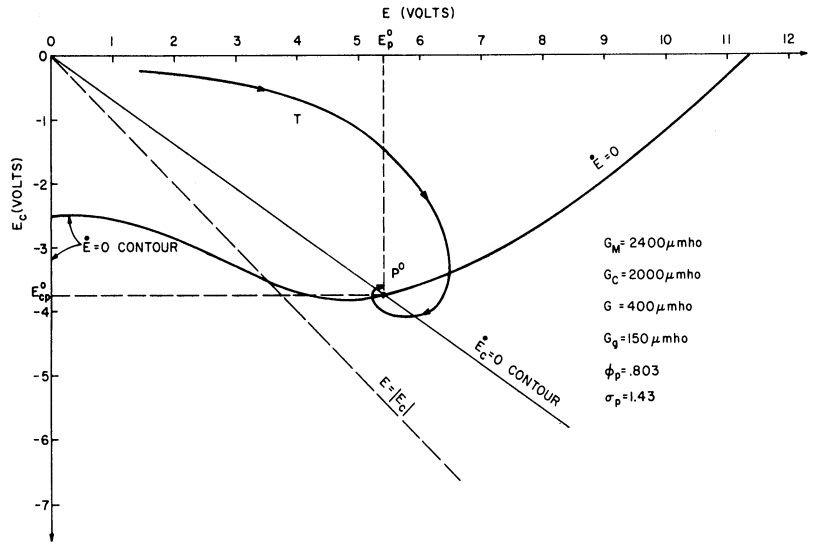

Fig. 10. Predicted $\dot{E} = 0$ and $\dot{E}_c = 0$ contours in the (E, E_c)-plane of the unforced oscillator when $G_g = 150$ μmho [note that $\dot{E} = 0$ along the entire E_c-axis--see (19)].

form of (27)

$$\omega(E_p^o, E_{cp}^o) - \nu = \frac{A}{2CE_p^o} \sin \theta_p . \tag{48}$$

Further simplification is obtained by noting that in the specific oscillator under consideration $\beta(E, E_c) << \omega_o$ in the vicinity of P^o and thus (48) may be approximately expressed as

$$\Delta = \frac{A}{2CE_p^o} \sin \theta_p , \tag{49}$$

where $\Delta = \omega_o - \nu$. Since (49) generally has two solutions in any interval of length 2π, there will be two equilibrium points on the $\dot{E} = 0$, $\dot{E}_c = 0$ intersection curve above P^o.

The forced system will also have an equilibrium point on the $\dot{E} = 0$, $\dot{E}_c = 0$ intersection line rising above the unstable equilibrium (at the origin) of the unforced system. This forced equilibrium point will be in the $\dot{E}_c = 0$ plane near the θ-axis and must be unstable since it is associated with an unstable point of the unforced system.

The equilibrium points of the forced system may be illustrated by taking a section (in the draftsman's sense) of the (E, E_c, θ)-phase space at the $\dot{E}_c = 0$ surface as shown in Fig. 11. The abscissa in this figure (distance along the $\dot{E}_c = 0$ surface) is ρE where $\rho = \sqrt{1 + m^2}$ and m is the slope of the $\dot{E}_c = 0$ contour in Fig. 10. The $\dot{\theta} = 0$ contour

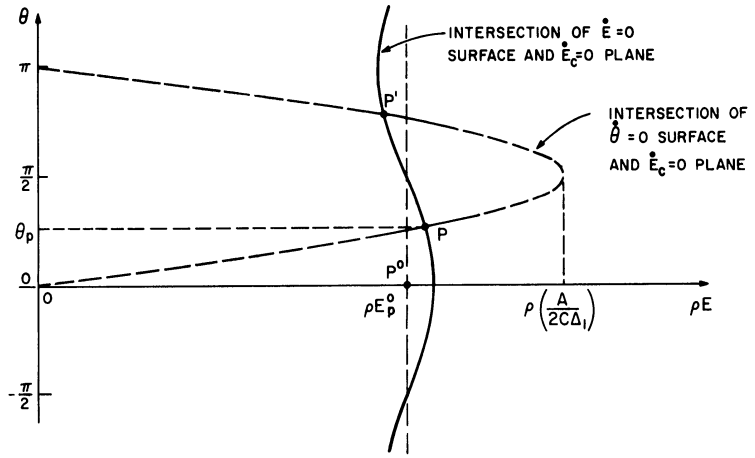

Fig. 11. Section of the (E, E_c, θ)-phase space along the $\dot{E}_c = 0$ surface (in this case the $\dot{E}_c = 0$ surface is a plane).

in this figure is the intersection of the $\dot{E}_c = 0$ plane and the $\dot{\theta} = 0$ surface

$$\rho E = \frac{\rho A}{2C\Delta} \sin \theta \ .$$

(The use of Δ is justified in this specific example because $\beta(E, E_c) << \omega_o$ along the $\dot{E}_c = 0$ plane where $2E^o_{cp} < E_c < 0.$) This $\dot{\theta} = 0$ contour intersects the $\dot{E}_c = 0$, $\dot{E} = 0$ intersection line rising above the two unforced equilibrium points at the three forced equilibrium points P, P', and P''.

As noted above, P'' will be unstable because it is associated with an unstable equilibrium point in the unforced system. On the other hand, since the unforced equilibrium point P^o is stable, the stability of the forced equilibrium points P and P' will be determined solely by the sign of $f_{3\theta}$ [see (33) for a related discussion] ; thus with A assumed positive and

$$f_{3\theta} = - \frac{A}{2C\bar{E}_p} \cos \theta \ ,$$

the lower intersection point P, where $\theta < \pi/2$, is stable while the upper point P', where $\theta > \pi/2$, is unstable. When the solution trajectories converge to the stable equilibrium point, E, E_c, and θ are constant and lock-in or frequency entrainment of the oscillator by the external signal is predicted. As the angular frequency difference, Δ, or the amplitude, A, of the external signal is changed, the $\dot{\theta} = 0$ sine curve changes amplitude. This, in turn, causes changes in the equilibrium-point locations, the oscillation amplitude E_p, and the relative phase θ_p. From the curves in Fig. 11 it is obviously quite easy to predict lock-in

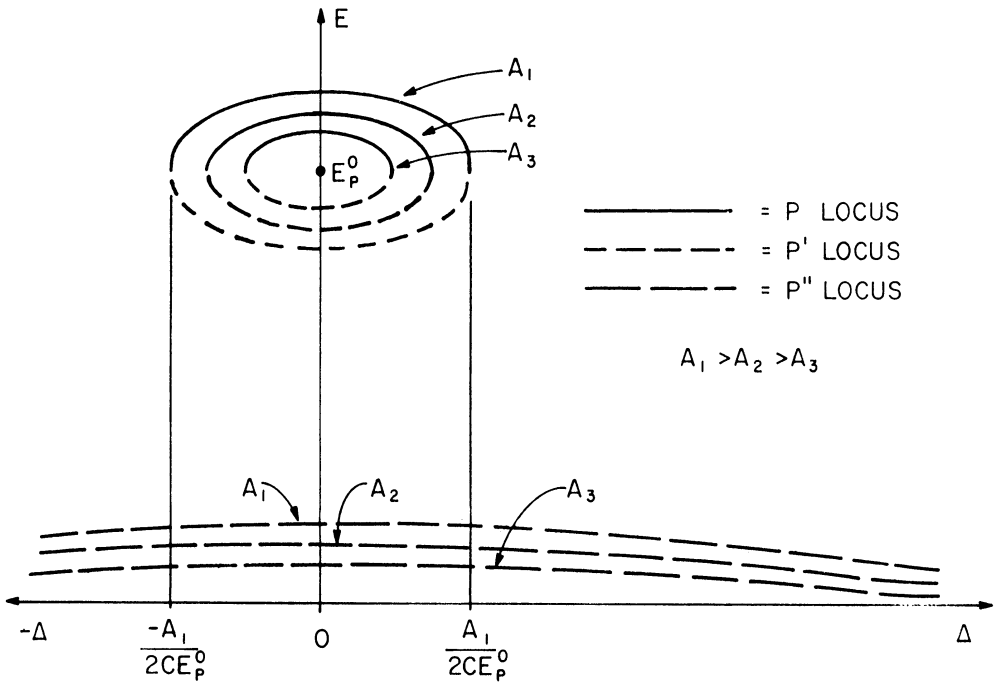

Fig. 12. Typical E vs. Δ equilibrium point locus.
Injected signal A as a parameter.

characteristics of the oscillator. For instance, Fig. 12 shows the form of the oscillation amplitude, E, versus angular frequency difference, Δ, locus of the three forced equilibrium points (injected signal amplitude A as a parameter) that would be obtained from Fig. 11. The similarity between Fig. 12 and the small signal lock-in curves of van der Pol (Ref. 8) is obvious.

The above discussion may be clarified by an examination of the solutions of a linearization of (19) and (20) in the vicinity of the equilibrium point P^o. If the new variables

$$x = E - E_p^o$$

and

$$y = E_c - E_{cp}^o \tag{50}$$

are introduced into the original model and the functions f_1 and f_2 are expanded about the point (E_p^o, E_{cp}^o), the resulting linearized model will give

$$\begin{cases} \dot{x} = f_{1E}x + f_{1E_c}y + \dfrac{A}{2C}\cos\theta, \\ \dot{y} = f_{2E_c}x + f_{2E_c}y, \\ \dot{\theta} = \Delta - \dfrac{A}{2CE_p^o}\sin\theta, \end{cases} \tag{51}$$

where, as before,

$$f_{ij} = \frac{\partial f_i}{\partial j} \text{ with } (i = 1, 2) \text{ and } (j = E, E_c)$$

but now the partial derivatives are evaluated at P^o. (These partial derivatives are computed in the Appendix.) When A = 0 the first two equations of (51) describe the behavior of the unforced system in a circular neighborhood of its equilibrium point. When A is nonzero but small, (51) describes the behavior of the forced system in an approximately cylindrical neighborhood of (0, 0, θ) in (x, y, θ)-space or of (E_p^o, E_{cp}^o, θ) in (E, E_c, θ)-space.

Now assume that (29) is satisfied so that lock-in occurs at $\theta = \theta_p$ where

$$\theta_p = \sin^{-1}\left(\frac{2CE_p^o\Delta}{A}\right) . \tag{52}$$

The angle θ is then fixed and the (x, y) coordinates of the equilibrium point (x_p, y_p) may be found as solutions of the system

$$\begin{cases} f_{1E}x_p + f_{1E_c}y_p + \dfrac{A}{2C}\cos\theta_p = 0, \\ f_{2E}x_p + f_{2E_c}y_p = 0. \end{cases} \tag{53}$$

This system can be solved for x_p. The solution gives

$$x_p = \left(\frac{f_{2E}}{f_{2E_c}}f_{1E_c} - f_{1E}\right)^{-1}\frac{A}{2C}\cos\left[\sin^{-1}\left(\frac{2CE_p^o\Delta}{A}\right)\right], \tag{54}$$

which is a complete description of the predicted lock-in curves for the stable equilibrium point P in terms of the amplitude and frequency difference of the injected signal. Typical curves are shown in Fig. 13 (these curves correspond to the P-locus in Fig. 12 with origin shifted up to E_p^o). These predicted lock-in curves of x_p vs. Δ were obtained from (54) for several values of A. Figure 13 also shows some observed (x_p, Δ) points from the experimental oscillator when it was locked-in with the external signal. The experimental oscillator parameters were adjusted to correspond to those assumed in (47) but failure to obtain

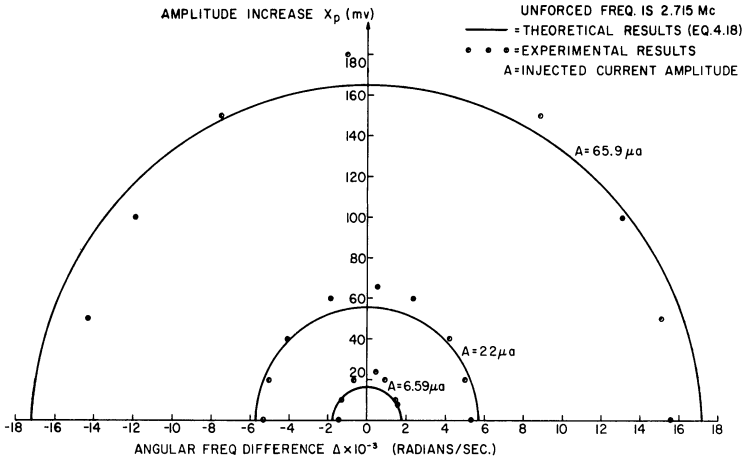

Fig. 13. Predicted and observed lock-in characteristics for oscillator with stable equilibrium point.

a perfect correspondence introduced some quantitative errors. Figure 14 shows a similar comparison between predicted and observed size of the (A, Δ)-plane lock-in region boundaries. Here the theoretical result was obtained from (29) with $\omega(E, E_c) = \omega_o$.

When (29) is not satisfied, $\theta(t)$ becomes a monotone function of time and a (E, E_c, θ) equilibrium point cannot exist. However, when A is small the second-order system described by the first two equations of (51) has a stable equilibrium for each fixed θ and the locus of these equilibrium points in (E, E_c, θ) space is the vertical cosinusoidal curve shown in Fig. 11. As $\theta(t)$ increases, the solution path might be expected to spiral around this equilibrium-point locus. This vertical spiral of the solution in (x, y, θ) or (E, E_c, θ)-space gives both an amplitude and phase modulation to e(t) which appears to correspond closely to the combination oscillations frequently described for nonlinear oscillators outside their lock-in region (Ref. 8). An analytic study at this point is complicated by the nonlinear dependence on θ in the first and third equations of (51). A graphical solution would be possible but lengthy. One case which can be treated simply occurs when $\Delta = \omega_o - \nu >> A/2CE_p$. For this case, $\dot{\theta} \approx \Delta$ and $\theta \approx \Delta t + \theta_o$. The remaining two equations are then

$$\begin{cases} \dot{x} = f_{1E}x + f_{1E_c}y + \dfrac{A}{2C}\cos(\Delta t + \theta_o), \\ \dot{y} = f_{2E}x + f_{2E_c}y, \end{cases} \tag{55}$$

which may be solved to give a steady-state solution

$$x(t) = \frac{A}{2C}\left[\frac{\Delta^2 + f_{2E_c}}{\Delta^4 + (2n + m^2)\Delta^2 + n^2}\right]^{\frac{1}{2}} \sin(\Delta t + \delta_1 + \delta_2 + \theta_o), \tag{56}$$

$$y(t) = \frac{A}{2C}\left[\frac{f_{2E}}{\Delta^4 + (2n + m^2)\Delta^2 + n^2}\right]^{\frac{1}{2}} \sin(\Delta t + \delta_2 + \theta_o), \tag{57}$$

where $m = f_{1E} + f_{2E_c}$ and $n = f_{1E_c} f_{2E} - f_{1E} f_{2E_c}$ are constants and δ_1 and δ_2 are functions of Δ.

When x and y are described by (56) and (57) and $\theta = \Delta t + \theta_o$, the (x, y, θ)-space solution trajectory is clearly a spiral around the θ-axis. Moreover, for large Δ the amplitude of the x variation is proportional to A/Δ while the frequency is $\Delta/2\pi$. Thus as Δ increases, the amplitude modulation in E goes to zero as $1/\Delta$ and E returns to the unforced value E_p^o. This corresponds closely with observed behavior of the experimental oscillator.

Although this does not exhaust the possible circumstances which may be encountered, the above discussion at least suggests that in several ways the model predicts behavior similar to that which would be observed in an oscillator operating in the presence of an external signal.

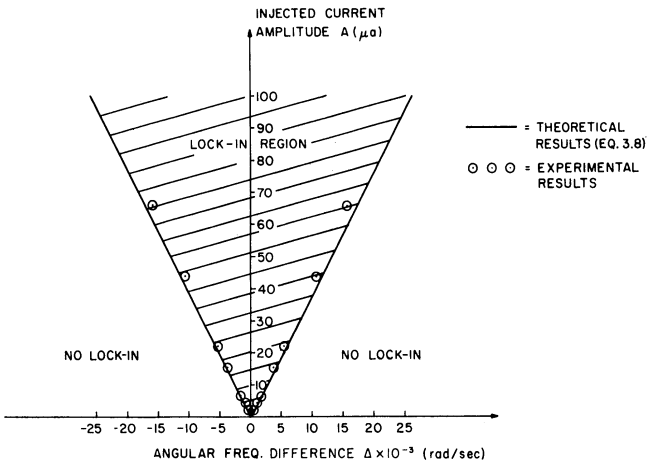

Fig. 14. Predicted and observed lock-in region boundaries in (A, Δ)-plane.

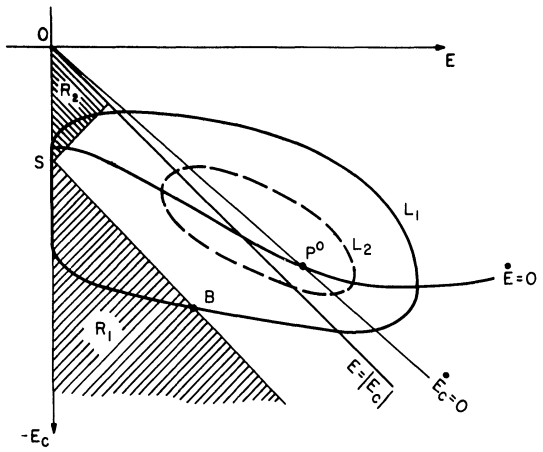

Fig. 15. Typical unforced system (E, E_c)-phase plane configuration showing limit cycles and regions R_1 and R_2.

4.3 Forced Oscillations When the Unforced System Has a Stable Limit Cycle

When G_g is small the (E, E_c)-phase plane of the unforced system contains one or more stable limit cycles. The typical example shown in Fig. 15 was drawn assuming the parameters of (47) with G_g = 25 μmho. Here the equilibrium point P^O is unstable and a stable limit cycle, L_1, encircling P^O is located approximately as shown. If P^O is stable, an additional unstable limit cycle, such as L_2, will occur between P^O and the stable limit cycle and bimodal operation will be possible. That is, the oscillator will operate either at P^O or on L_1 depending on initial conditions (see Ref. 1). In general, operation at P^O will result in a CW mode of oscillation and the forced behavior will be similar to that described in Section 4.2. On the other hand, operation on the stable limit cycle will produce an amplitude-modulated or squegging (pulsed) mode of oscillation and a completely new behavior in the presence of forcing signals. In this section, operation on a stable limit cycle in the presence of external signals will be considered.

When A = 0, the limit cycle is a solution path in the (E, E_c)-phase plane which is closed on itself. When A is nonzero but $\theta(t)$ is known, (19) and (20) can still be assumed to describe the motions of a second-order system in the phase plane; however, a disturbance from the $(A/2C)\cos\theta$ term has been added. If A is small, this disturbance will be negligible except when $(E/2C)(G_m^{hf} - G_c^{hf} - G)$ is small; that is, in the vicinity of the $\dot{E} = 0$ contour of the unforced system. It is important to note here that the unforced system $\dot{E} = 0$ contour has

two parts: the first part is the curve marked $\dot{E} = 0$ in Fig. 15 which passes through point P^o and the second part is the E_c-axis. If the particular stable limit cycle is a small curve enclosing P^o (such as L_2 in Fig. 15), it may never approach this second part of the $\dot{E} = 0$ contour. Thus in this case, the effects of small external signals will be limited to slight changes in the shape and location of the limit cycle through modification of the $\dot{E} = 0$ surface near the $\dot{E} = 0$ curve. However, a large limit cycle like L_1 in Fig. 15 remains in the vicinity of the second part of the $\dot{E} = 0$ contour over a consierable portion of its length. It will be shown that in this region the external signal may have a marked effect on the oscillations. Moreover, the magnitude of this effect will be related to the closeness of approach of the limit cycle to the E_c-axis (i. e., the minimum value of E along the limit cycle).

In general it is not possible to solve the equations (19), (20), and (21) to obtain a complete analytical description of a limit cycle. However, for a specific unforced oscillator the limit cycle can be drawn in the (E, E_c)-phase plane by standard numerical techniques. Moreover, for the specific oscillator considered in this section, analytic solutions may be obtained when E and E_c are in regions R_1 and R_2 of Fig. 15. This fact, coupled with the assumption that (E, E_c) coordinates of the forced-solution paths lie near the same coordinates of the unforced-solution paths, except near the $\dot{E} = 0$ contour, facilitates a piecewise description of several interesting limit cycles of the forced system.

Consider a solution path (possible limit cycle) which enters the region R_1 at point B with coordinates (E_B, E_{cB}, θ_B). From Section 4. 1, it can be seen that in region R_1, $i(e_c) = i_c(e_c) = 0$ and thus $G_m^{hf} = G_c^{hf} = G_c^{\ell f} = 0$ and

$$\omega(E, E_c) = \omega_o - \frac{G_g^{\,2}}{2CC_g\omega_o}. \tag{58}$$

Since the second term on the right in (58) is much smaller than ω_o [using the parameters (47)], the approximation $\omega(E, E_c) = \omega_o$ will be used in R_1. The simplified mathematical model is then

$$\begin{cases} \dot{E} = -\dfrac{E}{2C} G + \dfrac{A}{2C} \cos\theta, \\ \dot{E}_c = -\dfrac{E_c}{C_g} G_g, \\ \dot{\theta} = \omega_o - \nu - \dfrac{A}{2CE} \sin\theta. \end{cases} \tag{59}$$

The second equation of (59) gives

$$E_c = E_{cB} \exp\left[-\frac{G_g}{C_g} t\right] . \tag{60}$$

The first and third equations can be solved simultaneously using the technique described in the Appendix to give

$$e(t) = E(t) \cos[\nu t + \theta(t)] = E_B \exp\left[-\frac{G}{2C} t\right] \cos(\omega_o t + \theta_A)$$

$$+ \frac{1}{2C} \exp\left[-\frac{G}{2C} t\right] \int_o^t A(\xi) \exp\left[\frac{G}{2C} \xi\right] \cos[\omega_o t - (\omega_o - \nu)\xi] \, d\xi \quad .$$

However, when

$$\left|\frac{\dot{A}}{A}\right| T_L << 1 ,$$

where T_L is the limit cycle traversal time (pulse repetition period), the $A(\xi)$ in the integral is approximately constant and e(t) may be written as

$$e(t) = \exp\left[-\frac{G}{2C} t\right] \sqrt{E_o^2 + \frac{A\left[\frac{A}{2C} - \frac{G}{2C} E_B \cos\theta_B - (\omega_o - \nu) E_B \sin\theta_B\right]}{C\left[\left(\frac{G}{2C}\right)^2 + (\omega_o - \nu)^2\right]}} \cos(\omega_o t + \eta_1 + \eta_2)$$

$$+ \frac{A}{2C\sqrt{\left(\frac{G}{2C}\right)^2 + (\omega_o - \nu)^2}} \cos(\nu t + \eta_1) , \tag{61}$$

where

$$\eta_1 = \tan^{-1}\left[\frac{2C(\omega_o - \nu)}{G}\right] ,$$

and

$$\eta_2 = \tan^{-1}\left[\frac{\frac{G}{2C}\sin\theta_B - (\omega_o - \nu)\cos\theta_B}{\frac{G}{2C}\cos\theta_B + (\omega_o - \nu)\sin\theta_B - \frac{A}{2CE_B}}\right]$$

Equations (60) and (61) now describe the solution path in region R_1. The result is clearly a curve starting at B and tending upward and to the left (in Fig. 15) as E decreases and E_c increases. The next step is to determine the specific character of the trajectory in this region; that is, whether E or E_c decays faster.

Here it will be assumed that $C_g/G_g >> 2C/G$ (i. e., the grid-leak time

constant is much larger than the reciprocal of the tank damping). This assumption insures that a limit cycle similar to L_1 (as opposed to L_2) in Fig. 15 is being considered; that is, that the first term in (61) decays much faster than E_c and the solution path approaches E_c-axis (assuming small A). Thus the first term in (61) will be negligible by the time the solution reaches the upper edge of region R_1 and at this edge

$$\begin{cases} E = \dfrac{A}{2C\left\{\left[\dfrac{G}{2C}\right]^2 + (\omega_o - \nu)^2\right\}^{\frac{1}{2}}}, \\ \theta = \eta_1, \\ E_c = S. \end{cases} \tag{62}$$

These values will now be used as initial conditions in region R_2.[6] Note that they are independent of initial conditions at point B. This is because the term in (61) dependent on initial conditions has had time to decay to a negligible value.

In region R_2 the model is complicated by the fact that $i(e_c)$ is no longer zero. Examination of (43) reveals that in R_2, $G_m^{hf} = G_m + KE_c$ so that the simplified model is now

$$\begin{cases} \dot{E} = \dfrac{E}{2C}[G_m + KE_c - G] + \dfrac{A}{2C}\cos\theta, \\ \dot{E}_c = -\dfrac{E_c}{C_g} G_g, \\ \dot{\theta} = \omega(E, E_c) - \nu - \dfrac{A}{2CE}\sin\theta, \end{cases} \tag{63}$$

with initial conditions given by (62).

In the third equation of (63)

$$\omega(E, E_c) = \omega_o + \beta(E, E_c),$$

where

$$\beta(E, E_c) = \frac{G_g}{2CC_g\omega_o}[G_m + KE_c - G_g].$$

---

[6] Between region R_1 and R_2 is a wedge-shaped transition region where G_m^{hf} increases from 0 to its R_2 value of $G_m + KE_c$. However, when A is small $E_c \approx S$ at the lower edge of R_2 and since $K = -G_m/S$, the value of G_m^{hf} at the lower edge of R_2 is zero. Thus, for small A this transition region has little effect on the solution trajectories and may be ignored by assuming a direct transition from R_1 to R_2 along the line $E_c = S$.

For the parameters considered here $-180 < \beta < 3600$ in region R_2 and $\omega_o = 18 \times 10^6$. Thus the approximation $\omega(E, E_c) = \omega_o$ will be used.

Integration of the second equation of (63) and substitution into the first reveals that in region R_2 the solution path is now described by the time varying system

$$\begin{cases} \dot{E} = \frac{E}{2C}\left\{G_m - G - G_m \exp\left[-\frac{G_g}{C_g} t\right]\right\} + \frac{A}{2C} \cos\theta, \\ \dot{\theta} = \omega_o - \nu - \frac{A}{2CE} \sin\theta, \\ E_c = S\exp\left[-\frac{G_g}{C_g} t\right], \end{cases} \tag{64}$$

with initial conditions at time $t = 0$ given by (62). Note that the first term of E is initially negative but becomes positive as the exponential term decreases. This suggests that E will first decrease and then increase. Since E_c continues to increase in region R_2, the solution path should move up and to the right after the initial decrease in E.

A simultaneous solution of the $\dot{E}$ and $\dot{\theta}$ equations may again be obtained through the procedure described in the Appendix. The result is

$$\begin{aligned} e(t) = {} & E_o \exp\left[\frac{1}{2C} \int_o^t G_T(\alpha) d\alpha\right] \cos(\omega_o t + \theta_o) \\ & + \frac{1}{2C} \int_o^t A(\xi) \exp\left[\frac{1}{2C} \int_\xi^t G_T(\alpha) d\alpha\right] \cos[\omega_o t - (\omega_o - \nu)\xi] \, d\xi \end{aligned} \tag{65}$$

where $G_T(t)$ is the time-varying conductance

$$G_T(t) = G_m\left\{1 - \exp\left[-\frac{G_g}{C_g} t\right]\right\} - G, \tag{66}$$

and E_o and θ_o are the initial conditions given by (62). The two terms in e(t) are clearly related to the initial conditions and the forcing signal, respectively. In addition, the second term has several interesting features which are revealed in the following development.

First define

$$I = \frac{1}{2C} \int_o^t A(\xi) \exp\left\{\frac{1}{2C} \int_\xi^t G_T(\alpha) \, d\alpha\right\} \cos[\omega_o t - (\omega_o - \nu)\xi] \, d\xi \, . \tag{67}$$

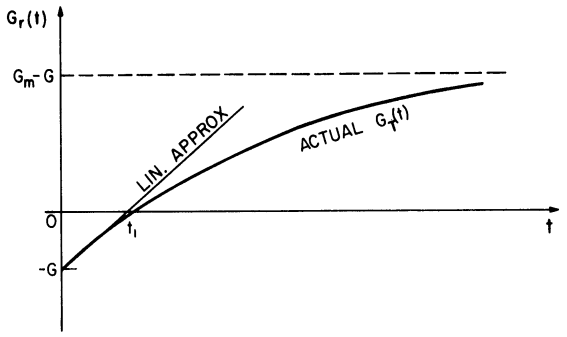

Fig. 16. Conductance function $G_T(t)$ vs. t and a linear approximation.

An examination of the conductance $G_T(t)$ reveals the exponential function shown in Fig. 16. However, for times which are small compared to C_g/G_g (which is 40 μsec in this example) the conductance variation of (66) is accurately approximated by

$$G_T(t) \approx G_m \frac{G_g}{C_g} t - G . \tag{68}$$

This approximation is also shown in Fig. 16 with the time t_1 when $G_T(t) = 0$ now given as

$$t_1 = \frac{GC_g}{G_m G_g} . \tag{69}$$

In order to understand the importance of t_1 it is necessary to introduce the change of variable $z = \xi - t_1$ into (67) given

$$I = \frac{1}{2C} \exp\left\{\frac{1}{2C} \int_{t_1}^{t} G_T(\alpha)\, d\alpha\right\} \int_{-t_1}^{t-t_1} A(\xi) \exp\left\{-\frac{1}{2C} \int_{t_1}^{z+t_1} G_T(\alpha)\, d\alpha\right\} \cos\left[\omega_o t - (\omega_o - \nu)(z + t_1)\right] dz. \tag{70}$$

The inner integral can now be integrated using (68) and (69) so that

$$I = \frac{1}{2C} \exp\left\{\frac{1}{2C} \int_{t_1}^{t} G_T(\alpha)\, d\alpha\right\} \int_{-t_1}^{t-t_1} A(\xi) \exp\left\{-\frac{G}{4Ct_1} z^2\right\} \cos\left[\omega_o t - (\omega_o - \nu)(z + t_1)\right] dz . \tag{71}$$

Here it is immediately noted that the exponential term in the integrand of the second integral is like a Gaussian probability density function with zero mean and variance $4Ct_1/G$. If this variance is small compared with t_1, the integrand of the second integral is zero except near the time $z = 0$ or $t = t_1$. It is during this time that the oscillator "samples the forcing function" and "decides" how its behavior will be effected by the external signal. Thus, when A

is a slowly varying function of time, only $A(t_1)$ would be seen by the oscillator.

In addition to this sampling operation, the occurrence of the $\exp\left\{-\frac{G}{4Ct_1}z^2\right\}$ term allows an approximation by the infinite integral when the variance is small. In this case

$$I \approx \frac{1}{2C}\exp\left\{\frac{1}{2C}\int_{t_1}^{t} G_T(\alpha)\,d\alpha\right\}\int_{-\infty}^{\infty} A(t_1)\exp\left\{-\frac{G}{4Ct_1}z^2\right\}\cos\left[\omega_o t - (\omega_o - \nu)(z + t_1)\right]\,dz\ . \tag{72}$$

Expansion of the cosine term gives

$$\cos(\omega_o t - \Lambda)\cos(\omega_o - \nu)z + \sin(\omega_o t - \Lambda)\sin(\omega_o - \nu)z \tag{73}$$

where $\Lambda = (\omega_o - \nu)t_1$. Here, the fact that

$$\exp\left[-\frac{G}{4Ct_1}z^2\right]\sin(\omega_o - \nu)z$$

is an odd function of Z, allows the second term in (73) to be omitted so that

$$I \approx \frac{1}{2C}\exp\left\{+\frac{1}{2C}\int_{t_1}^{t} G_T(\alpha)\,d\alpha\right\}\left[\int_{-\infty}^{\infty} A(t_1)\exp\left\{-\frac{G}{4Ct_1}z^2\right\}\cos(\omega_o - \nu)z\,dz\right]\cos(\omega_o t - \Lambda)\ . \tag{74}$$

The second integral can now be evaluated giving

$$I \approx A(t_1)\sqrt{\frac{\pi t_1}{4GC}}\left[\exp\left\{\frac{1}{2C}\int_{t_1}^{t} G_T(\alpha)\,d\alpha\right\}\right]\left[\exp\left\{-\frac{t_1 C}{G}(\omega_o - \nu)^2\right\}\right]\cos(\omega_o t - \Lambda)\ . \tag{75}$$

The complete expression for e(t) may now be written

$$e(t) = \left[\exp\left\{\frac{1}{2C}\int_{o}^{t} G_T(\alpha)\,d\alpha\right\}\right]\frac{A(t_1)}{2C\left[\left(\frac{G}{2C}\right)^2 + (\omega_o - \nu)^2\right]^{\frac{1}{2}}}\cos(\omega_o t + \eta_1)$$

$$+ A(t_1)\sqrt{\frac{\pi t_1}{4GC}}\left[\exp\left\{\frac{1}{2C}\int_{t_1}^{t} G_T(\alpha)\,d\alpha\right\}\right]\left[\exp\left\{-\frac{t_1 C}{G}(\omega_o - \nu)^2\right\}\right]\cos(\omega_o t - \Lambda)\ . \tag{76}$$

where the initial conditions from (62) have been used. The first term in (76) is caused by the initial condition and its amplitude will be denoted $E_i(t)$; the second term is caused by the forcing signal and its amplitude will be denoted $E_f(t)$. Note that both are amplitude modulated cosines at the natural frequency ω_o; that is, there is no lock-in or other center frequency shift introduced by the external signal. Only amplitude changes are affected. The relative importance of these two terms may be seen from the amplitude ratio

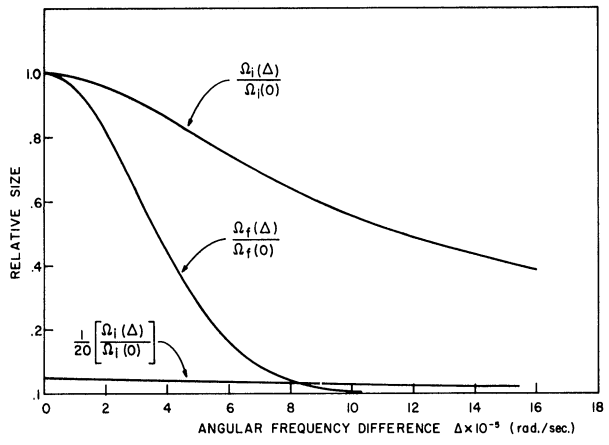

Fig. 17. Comparison of two frequency dependent terms in the forced response.

$$\frac{E_f(t)}{E_i(t)} = \sqrt{\frac{\pi C_g C}{G_m G_g}} \exp\left\{ -\frac{1}{2C} \int_0^{t_1} G_T(\alpha)\, d\alpha \right\} \left[\frac{\Omega_f(\Delta)}{\Omega_i(\Delta)} \right], \tag{77}$$

where Ω_f and Ω_i terms represent the frequency dependent parts of E_f and E_i, respectively. At resonance, $\Delta = \omega_o - \nu = 0$, $\Omega_f(\Delta) = 1$, and $\Omega_i(\Delta) = \frac{2C}{G}$ so that the ratio of (77) becomes

$$\left.\frac{E_f(t)}{E_i(t)}\right|_{\Delta=0} = \sqrt{\frac{\pi C_g G^2}{4C G_m G_g}} \exp\left\{ -\frac{1}{2C} \int_0^{t_1} G_T(\alpha)\, d\alpha \right\} \tag{78}$$

With the parameters assumed in this section, E_f is about 20 times as large as E_i near resonance. Away from resonance, the relative size changes due to the different frequency dependence of the Ω_f and Ω_i terms shown in Fig. 17. Note that the two frequency response curves can be adjusted independently since the bandwidth of E_i depends on the normal tank loading G and the bandwidth of E_f depends on the negative conductance G_m.

With the aid of (76) it is possible to compute the location of the solution path in region R_2. If the E_i term is neglected the operation in this region is given by

$$\begin{cases} E(t) = E_f(t) = A(t_1) \sqrt{\frac{\pi t_1}{4GC}} \left[\exp\left\{ \frac{1}{2C} \int_{t_1}^{t} G_T(\alpha)\, d\alpha \right\} \right] \left[\exp\left\{ -\frac{t_1 C}{G} (\omega_o - \nu)^2 \right\} \right], & (79) \\ E_c(t) = S \left[\exp\left\{ -\frac{G_g}{C_g} t \right\} \right], & (80) \\ \theta(t) = (\omega_o - \nu)t - \Lambda . & (81) \end{cases}$$

This solution path moves up and to the right in R_2, as suggested in Fig. 15, and leaves R_2 along one of the lines $E = -E_c$ or $E = E_c - \mathcal{S}$. In either case the exact point may be located from (79) and (80).

Solutions for $E(t)$ and $E_c(t)$ that are outside of R_2 are not so easily obtained. However, in this region the forcing term in (19) is seen to be small compared to the first term suggesting that the unforced phase-plane solution may be used to continue the solution back to region R_1. This permits a more accurate estimate of the entrance point (E_B, E_{cB}) and eventually leads to a description of the (E, E_c)-plane projection of the entire forced limit cycle.

In the above development it was assumed that $G_g/C_g << G/2C$ so that the first term in (61) could be neglected leading to simplified initial conditions at entry into region R_2. Without this assumption the evaluation of the behavior in region R_2 is considerably complicated. The E_i term may then become much more important with new frequency dependent effects appearing. These effects are commonly encountered in superregenerative devices where remnant energy carry-over between pulses is obtained.

Once again, the development presented does not exhaust the possible behavior which may be encountered. However, it does present some interesting features of the model which appear to correspond closely with commonly observed behavior in forced, self-biased oscillators. It also suggests that further study of the model may bring out this correspondence in greater detail.

4.4 Sensitivity and Superregenerative Detection

At this point it is of interest to consider the results of the previous section in greater detail through an application to superregenerative detector analysis. The situation considered in Section 4.3, where the unforced oscillator has a stable limit cycle passing close to the E_c-axis, is clearly a classic example of a self-quenched superregenerative detector. Moreover, a slight modification in approach leads to an extension of the analysis to externally quenched, logarithmic (nonlinear) superregenerative detectors. Basically, this extension amounts to a modification of (20) so that E_c has the form of the chosen quench signal. For most reasonable quench signals, small forcing signals will still be effective only during the pulse growth period (region R_2 or its equivalent) and thus (63),

with the proper E_c quench signal, will still describe many of the interesting detector characteristics. Further analysis of external quenching will not be pursued in this paper but a short discussion of self-quenched operation will be given below both as an interesting application and as a further means of checking the validity of the mathematical model through comparison with experimental results.

The two superregenerative detector characteristics of central interest in this section are sensitivity and bandwidth. These two characteristics are not only important in application but also easily measured experimentally. Moreover, because it is readily obtained from the mathematical model, the maximum value of the low frequency grid voltage waveform is chosen as the desired detector output (many others are of course possible). This output voltage, denoted E_{cm}, is the upper intersection of the limit cycle and the $\dot{E}_c = 0$ line in Fig. 15. While this intersection is not actually in R_2, due to its proximity to R_2, the R_2 relations (79) and (80) will be used to approximate E_{cm}. The shape of the $\dot{E}_c$ and $\dot{E}$ contours in this region suggests that this approximation should be fairly accurate.

The location of the E_{cm} point may be deduced from the fact that on the $\dot{E}_c = 0$ surface, $E = mE_c$ where m is the slope of the $\dot{E}_c = 0$ line (see Fig. 15). The time t_2 at which $E = mE_c$ is obtained from (79) and (80) as follows:

$$t_2 = t_1 - \frac{2C}{G_m} + \sqrt{\left(\frac{2C}{G_m}\right)^2 + \frac{4CC_g}{G_m G_g} \ln \left\{ \frac{-\frac{S}{m} \exp\left\{-\frac{G_g}{C_g} t_1\right\}}{A \frac{\pi C_g}{4CG_m G_g}} \left[\exp\left\{\frac{CC_g}{G_m G_g} (\omega_o - \nu)^2\right\}\right] \right\}} \quad (82)$$

This t_2 may now be substituted into (80) to obtain E_{cm} as a function of A and ν or $\Delta = \omega_o - \nu$. A plot of E_{cm} vs. A with Δ as a parameter is shown in Fig. 18 (in this section $\dot{A} = 0$). Figure 18 also shows observed values of E_{cm} vs. A obtained from the experimental oscillator. The theoretical detector bandwidth obtained from (82) is plotted in Fig. 19 along with corresponding experimental results. Note that both (82) and Fig. 18 show that the only effect of injected signal frequency offset is an attentuation at the detector output. Thus, for smaller signal amplitudes, curves like Fig. 18 would be similar in shape but smaller. A related effect may be noted in both Figs. 18 and 19 where the experimental and theoretical results follow quite closely except when the injected signal is small or, equivalently, the

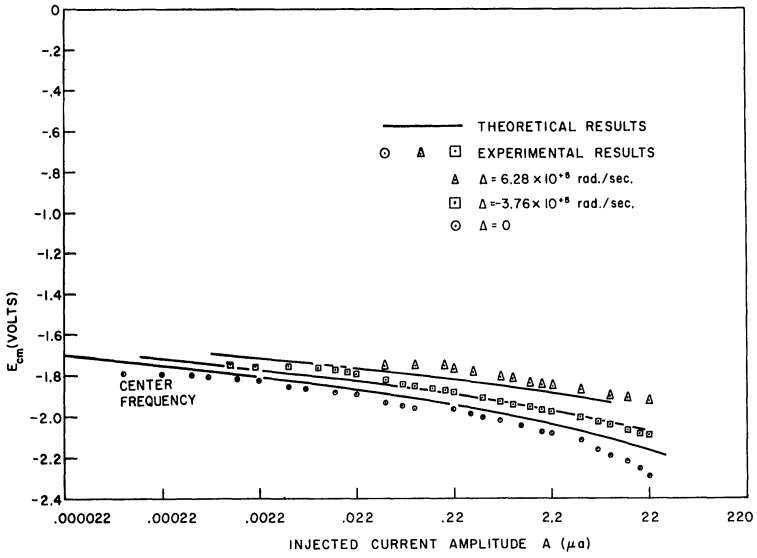

Fig. 18. Comparison of predicted and observed detector output E_{cm} versus injected signal amplitude A at several frequency separations Δ.

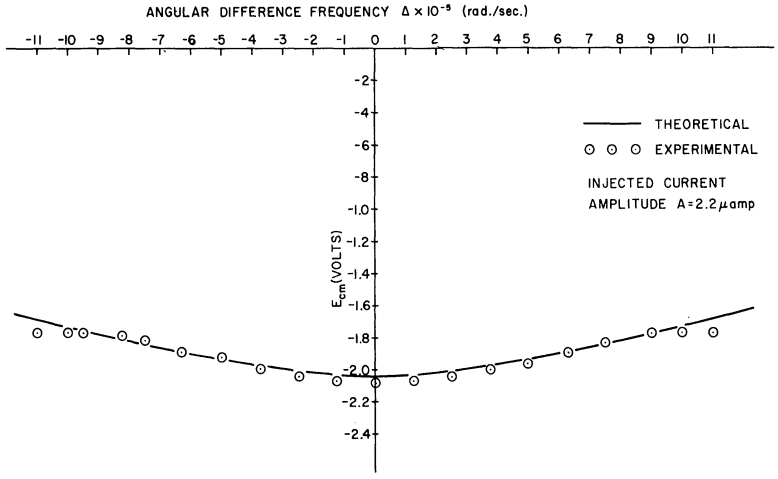

Fig. 19. Detector output E_{cm} versus frequency separation Δ with fixed injected signal amplitude.

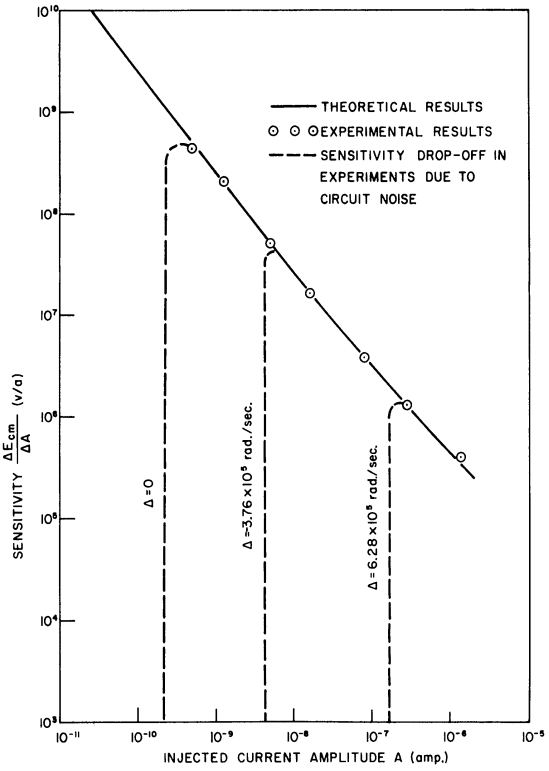

Fig. 20. Predicted and observed sensitivity of E_{cm} to changes in A showing decrease in observed sensitivity at several values of frequency separation Δ.

frequency difference is large. Both of these departures are due to the small injected noise signal always present in the experimental oscillator but not considered in the theoretical analysis. Thus, by noting the location of the "break-away," one can estimate the magnitude of this circuit noise.

In this paper the ratio $\Delta E_{cm}/\Delta A$ is defined as the sensitivity of E_{cm} to changes in A and is related to the superregenerative detector sensitivity through the signal source or antenna impedance. The plot of sensitivity vs. A in Fig. 20 emphasizes the inherent nonlinearity of the detector and the sensitivity limitation imposed by the circuit noise level. Once again the experimentally determined sensitivity is presented for comparison with the results predicted by the model.

5. CONCLUSIONS

This paper has been concerned with the development and interpretation of a mathematical model for a class of self-biased oscillators operating under the influence of an external signal. The devices considered differ from previously studied oscillators in that two arbitrary nonlinear elements are allowed (for instance, both the plate and grid circuits of a vacuum tube). This model is therefore more general than previous forced oscillator models based on the van der Pol equation. The model obtained is a system of three first-order nonlinear differential equations chosen to approximate the more complex equations obtained directly from the basic equivalent circuit.

The complexity of the mathematical model makes a complete analysis impractical but several interesting features are investigated in some detail. These include frequency entrainment by the forcing signal and superregenerative detector action. In each case the theoretical results are corroborated by the observed behavior of an experimental oscillator.

The close correlation between theoretically predicted and experimentally observed behavior found throughout the analysis suggest that the proposed model does indeed provide a suitable compromise between accuracy and tractability in the modeling of forced oscillation in self-biased oscillators.

APPENDIX

A. Approximation Procedures

The approximating system (9) is developed from an averaging procedure suggested by the work of Krylov, Bogoliubov, and Mitropolsky (Ref. 2). The transformed system (8) may be written in simplified form as

$$\begin{cases} \dot{E} = h_1(E, E_c, \gamma, \theta, A), \\ \dot{E}_c = h_2(E, E_c, \gamma, \theta, A), \\ \dot{\gamma} = h_3(E, E_c, \gamma, \theta, A), \end{cases} \tag{83}$$

where h_1, h_2, and h_3 are periodic in γ with period 2π. Now assume that for time intervals near $2\pi/\omega_o$ (recall that $\omega_o = 1/\sqrt{LC}$), $e_c(t) = E_c(t) + E(t) \cos \gamma(t)$ is locally cosinusoidal and A(t) is approximately constant. That is, in such intervals $e_c(t) \approx E_c + E \cos(\nu t + \theta)$ and $A(t) \approx A$ where E, E_c, ν, θ, and A are constants. This assumption of slowly varying parameters motivates the averaging and regrouping of terms in the three equations (83) giving

$$\frac{F_i(t+T) - F_i(t)}{T} = \frac{1}{T} \int_t^{t+T} h_i(E, E_c, \lambda, \theta, A)\, d\xi$$

$$+ \frac{1}{T} \int_t^{t+T} \left\{ h_i[E(\xi), E_c(\xi), \gamma(\xi), \theta(\xi), A(\xi)] - h_i(E, E_c, \lambda, \theta, A) \right\} d\xi \tag{84}$$

for i = 1, 2, 3 with $F_1 = E$, $F_2 = E_c$, $F_3 = \gamma$, and $\lambda = \nu\xi + \theta$. It is now assumed that the approximations $E_c + E \cos(\nu t + \theta)$ and A are sufficiently close to $e_c(t)$ and A(t) over the integration interval to justify ignoring the second integral in each of the three (84) equations.

Since the h_i's are periodic in λ, setting $T = 2\pi/\gamma$ allows (84) to be rewritten as

$$\frac{\Delta F_i}{\Delta t} = \frac{1}{2\pi} \int_o^{2\pi} h_i(E, E_c, \lambda, \theta, A)\, d\lambda = f_i(E, E_c, \theta, A), \tag{85}$$

for i = 1, 2, 3 where the substitutions $\Delta F_i = F_i(t+T) - F_i(t)$ and $\Delta t = T$ have been used. The final step is to replace (85) by the system of differential equations

$$\begin{cases} \dot{E} = f_1(E, E_c, \theta, A), \\ \dot{E}_c = f_2(E, E_c, \theta, A), \\ \dot{\gamma} = f_3(E, E_c, \theta, A). \end{cases} \tag{86}$$

The system (86) is then chosen as an approximation to (83).

B. Stability of Equilibrium Points

The stability of an equilibrium point may be determined from the characteristic roots of the linearized system. For the oscillator model

$$\begin{cases} \dot{E} = f_1(E, E_c, \theta), \\ \dot{E} = f_2(E, E_c), \\ \dot{\theta} = f_3(E, E_c, \theta), \end{cases} \tag{87}$$

the characteristic roots are the roots of the equation

$$\lambda^3 + (f_{1E} + f_{2E_c} + f_{3\theta})\lambda^2 + (f_{1E}f_{2E_c} + f_{1E}f_{3\theta} + f_{2E_c}f_{3E} - f_{1\theta}f_{3E} - f_{1E_c}f_{2E})\lambda$$

$$- f_{1E}f_{2E_c}f_{3\theta} - f_{1\theta}f_{2E}f_{3E_c} + f_{1\theta}f_{2E_c}f_{3E} + f_{1E_c}f_{2E}f_{3\theta} = 0$$

The coefficients of this equation are made up of the partial derivatives

$$f_{ij} = \frac{\partial f_i}{\partial j}\Bigg|_{\substack{E = E_p \\ E_c = E_{cp} \\ \theta = \theta_p}} \qquad (i = 1, 2, 3), \quad (j = E, E_c\theta)$$

evaluated at the equilibrium point (E_p, E_{cp}, θ_p). The coefficients of interest for the oscillator considered in Section 4 are

$$f_{1E} = \frac{G_m + KE_c}{2\pi C}\sin 2\sigma - \frac{G_c + KE_c}{2\pi C}\sin 2\phi \tag{88}$$

$$+ \frac{EK}{3\pi C}[2\sin\sigma + \cos 2\sigma \sin\sigma - 2\sin\phi - \cos 2\phi \sin\phi],$$

$$f_{1E_c} = 2\left(\frac{G_m + KE_c}{2\pi C}\right)\sin\sigma - 2\left(\frac{G_c + KE_c}{2\pi C}\right)\sin\phi + \frac{KE}{2\pi C}[h(\sigma) - h(\phi)], \tag{89}$$

$$f_{2E} = -\frac{G_c}{\pi C_g}\sin\phi, \tag{90}$$

$$f_{2E_c} = -\frac{G_g}{C_g} - \frac{G_c}{\pi C_g}\phi \,, \tag{91}$$

$$f_{3\theta} = -\frac{A}{2CE}\cos\theta \,, \tag{92}$$

where $h(x) = x + \frac{1}{2}\sin 2x$ and parameters E, E_c, σ and ϕ are all values measured at the equilibrium point in question.

For the unforced system the characteristic equation reduces to

$$\lambda^2 - (f_{1E} + f_{2E_c})\lambda - f_{1E_c}f_{2E} + f_{1E}f_{2E_c} = 0 \,. \tag{93}$$

C. Solution of a Differential Equation

In Section 4 it is necessary to solve a system of differential equations of the form

$$\begin{cases} \dot{E} = \alpha(t)\, E + \beta(t)\cos\theta \,, \\ \dot{\theta} = \gamma - \dfrac{\beta(t)}{E}\sin\theta \,. \end{cases} \tag{94}$$

A solution may be obtained by letting

$$z = u + jv = Ee^{j\theta} \tag{95}$$

so that

$$\begin{aligned} \dot{u} &= \dot{E}\cos\theta - E\dot{\theta}\sin\theta \,, \\ \dot{v} &= \dot{E}\sin\theta + E\dot{\theta}\cos\theta \,. \end{aligned} \tag{96}$$

Substitution of (94) into (96) then yields a differential equation in z of the form

$$\dot{z} = [\alpha(t) + j\gamma]\, z + \beta(t) \,. \tag{97}$$

This equation is readily solved by standard techniques yielding

$$z(t) = z(t_o)\exp\left\{\int_{t_o}^{t} [\alpha(\theta) + j\gamma]\, d\theta\right\} + \int_{t_o}^{t} \beta(\xi)\exp\left\{\int_{\xi}^{t} [\alpha(\theta) + j\gamma]\, d\theta\right\} d\xi \,. \tag{98}$$

Now E and θ may be obtained from the real and imaginary parts of z. However, in many cases it is more convenient to obtain e(t) directly from the relation

$$e(t) = \mathrm{Re}\left\{ z(t)e^{j\nu t}\right\} \,. \tag{99}$$

REFERENCES

1. F. N. Bailey and A. W. Naylor, "Analysis of a Class of Self-Biased Multimode Oscillators," IEEE Transactions on Circuit Theory, Vol. CT-10, No. 3, September 1963.

2. N. Krylov and N. Bogoliubov, Introduction to Nonlinear Mechanics, Princeton University Press, Princeton, New Jersey, 1943.

   N. Bogoliubov and Y. Mitropolsky, Asymptotic Methods in the Theory of Nonlinear Oscillations, Gordon and Breach, New York, N. Y., 1961.

3. J. R. Whitehead, Super-Regenerative Receivers, Cambridge University Press, 1950.

4. W. Kaplan, Advanced Calculus, Addison-Wesley, Reading, Massachusetts, 1952.

5. J. G. Truxal, Automatic Control System Synthesis, McGraw-Hill, New York, N. Y., 1955.

6. F. N. Bailey and A. W. Naylor, Analysis of a Class of Self-Biased Oscillators, Cooley Electronics Laboratory Technical Report No. 100, The University of Michigan, Ann Arbor, Michigan, January 1961.

7. N. Minorsky, Nonlinear Oscillations, Van Nostrand, Princeton, New Jersey, 1962.

8. J. J. Stoker, Nonlinear Vibrations, Interscience, New York, N. Y., 1950.

DISTRIBUTION LIST

Copy No.	
1-2	Commanding Officer, U. S. Army Electronics Research and Development Laboratory, Fort Monmouth, New Jersey, ATTN: Senior Scientist, Electronic Warfare Division
3	Commanding General, U. S. Army Electronic Proving Ground, Fort Huachuca, Arizona, ATTN: Director, Electronic Warfare Department
4	Chief, Research and Development Division, Office of the Chief Signal Officer, Department of the Army, Washington 25, D. C., ATTN: SIGEB
5	Commanding Officer, Signal Corps Electronic Research Unit, 9560th USASRU, P. O. Box 205, Mountain View, California
6	U. S. Atomic Energy Commission, 1901 Constitution Avenue, N. W., Washington 25, D. C., ATTN: Chief Librarian
7	Director, Central Intelligence Agency, 2430 E Street, N. W., Washington 25, D. C., ATTN: OCD
8	U. S. Army Research Liaison Officer, MIT-Lincoln Laboratory, Lexington 73, Massachusetts
9-18	Defense Documentation Center, Cameron Station, Alexandria, Virginia
19	Commander, Air Research and Development Command, Andrews Air Force Base, Washington 25, D. C., ATTN: SCEC, Hq.
20	Directorate of Research and Development, USAF, Washington 25, D. C., ATTN: Electronic Division
21-22	Hqs., Aeronautical Systems Division, Air Force Command, Wright-Patterson Air Force Base, Ohio, ATTN: WWAD
23	Hqs., Aeronautical Systems Division, Air Force Command, Wright-Patterson Air Force Base, Ohio, ATTN: WCLGL-7
24	Air Force Liaison Office, Hexagon, Fort Monmouth, New Jersey
25	Commander, Air Force Cambridge Research Center, L. G. Hanscom Field, Bedford, Massachusetts, ATTN: CROTLR-2
26-27	Commander, Rome Air Development Center, Griffiss Air Force Base, New York, ATTN: RCSSLD - For retransmittal to - Ohio State University Research Foundation
28	Commander, Air Proving Ground Center, ATTN: Adj/Technical Report Branch, Eglin Air Force Base, Florida
29	Chief, Bureau of Naval Weapons, Code RRR-E, Department of the Navy, Washington 25, D. C.

DISTRIBUTION LIST (Cont.)

Copy No.	
30	Chief of Naval Operations, EW Systems Branch, OP-35, Department of the Navy, Washington 25, D. C.
31	Chief, Bureau of Ships, Code 691C, Department of the Navy, Washington 25, D. C.
32	Chief, Bureau of Ships, Code 684, Department of the Navy, Washington 25, D. C.
33	Chief, Bureau of Naval Weapons, Code RAAV-33, Department of the Navy, Washington 25, D. C.
34	Commander, Naval Ordnance Test Station, Inyokern, China Lake, California, ATTN: Test Director - Code 30
35	Director, Naval Research Laboratory, Countermeasures Branch, Code 5430, Washington 25, D. C.
36	Director, Naval Research Laboratory, Washington 25, D. C., ATTN: Code 2021
37	Director, Air University Library, Maxwell Air Force Base, Alabama, ATTN: CR-4987
38	Commanding Officer - Director, U. S. Naval Electronics Laboratory, San Diego 52, California
39	Office of the Chief of Ordnance, Department of the Army, Washington 25, D. C., ATTN: ORDTU
40	Commanding Officer, U. S. Naval Ordnance Laboratory, Silver Spring 19, Maryland
41-42	Chief, U. S. Army Security Agency, Arlington Hall Station, Arlington 12, Virginia, ATTN: IADEV
43	President, U. S. Army Defense Board, Headquarters, Fort Bliss, Texas
44	President, U. S. Army Airborne and Electronics Board, Fort Bragg, North Carolina
45	U. S. Army Antiaircraft Artillery and Guided Missile School, Fort Bliss, Texas
46	Commander, USAF Security Service, San Antonio, Texas, ATTN: CLR
47	Chief, Naval Research, Department of the Navy, Washington 25, D. C., ATTN: Code 931
48	Commanding Officer, 52d U. S. Army Security Agency, Special Operations Command, Fort Huachuca, Arizona

DISTRIBUTION LIST (Cont.)

Copy No.

49 President, U. S. Army Security Agency Board, Arlington Hall Station, Arlington 12, Virginia

50 The Research Analysis Corporation, 6935 Arlington Rd., Bethesda 14, Maryland, ATTN: Librarian

51 Carlyle Barton Laboratory, The Johns Hopkins University, Charles and 34th Streets, Baltimore 18, Maryland

52 Stanford Electronics Laboratories, Stanford University, Stanford, California, ATTN: Applied Electronics Laboratory Document Library

53 HRB - Singer, Inc., Science Park, State College, Pennsylvania, ATTN: R. A. Evans, Manager, Technical Information Center

54 ITT Laboratories, 500 Washington Avenue, Nutley 10, New Jersey, ATTN: Mr. L. A. DeRosa, Div. R-15 Lab.

55 Director, USAF Project Rand, via Air Force Liaison Office, The Rand Corporation, 1700 Main Street, Santa Monica, California

56 Stanford Electronics Laboratories, Stanford University, Stanford, California, ATTN: Dr. R. C. Cumming

57 Stanford Research Institute, Menlo Park, California

58-59 Commanding Officer, U. S. Army Signal Missile Support Agency, White Sands Missile Range, New Mexico, ATTN: SIGWS-EW and SIGWS-FC

60 Commanding Officer, U. S. Naval Air Development Center, Johnsville, Pennsylvania, ATTN: Naval Air Development Center Library

61 Commanding Officer, U. S. Army Electronics Research and Development Laboratory, Fort Monmouth, New Jersey, ATTN: U. S. Marine Corps Liaison Office, Code AO-C

62 Director, Fort Monmouth Office, Communications-Electronics Combat Development Agency, Bldg. 410, Fort Monmouth, New Jersey

63-71 Commanding Officer, U. S. Army Electronics Research and Development Laboratory, Fort Monmouth, New Jersey

ATTN:
- 1 Copy — Director of Research
- 1 Copy — Technical Documents Center ADT/E
- 1 Copy — Chief, Special Devices Branch, Electronic Warfare Div.
- 1 Copy — Chief, Advanced Techniques Branch, Electronic Warfare Div.
- 1 Copy — Chief, Jamming and Deception Branch, Electronic Warfare Div.
- 1 Copy — File Unit No. 2, Mail and Records, Electronic Warfare Div.
- 3 Cpys — Chief, Security Division (For retransmittal to - EJSM)

DISTRIBUTION LIST (Cont.)

Copy No.	
72	Director, National Security Agency, Fort George G. Meade, Maryland, ATTN: TEC
73	Dr. B. F. Barton, Director, Cooley Electronics Laboratory, The University of Michigan, Ann Arbor, Michigan
74-97	Cooley Electronics Laboratory Project File, The University of Michigan, Ann Arbor, Michigan
98	Project File, The University of Michigan Office of Research Administration, Ann Arbor, Michigan
99	Bureau of Naval Weapons Representative, Lockheed Missiles and Space Co., P. O. Box 504, Sunnyvale, California - For forwarding to - Lockheed Aircraft Corp.
100	Lockheed Aircraft Corp., Technical Information Center, 3251 Hanover Street, Palo Alto, California

Above distribution is effected by Electronic Warfare Division, Surveillance Department, USAELRDL, Evans Area, Belmar, New Jersey. For further information contact Mr. I. O. Myers, Senior Scientist, Telephone 5961262